November 1990 UILU-ENG-90-2254

EFFICIENT EVALUATION OF THE INNER PRODUCTS IN THE SPECTRAL DOMAIN ANALYSIS OF MICROSTRIP DISCONTINUITIES

Dan McNay
Raj Mittra

Coordinated Science Laboratory
College of Engineering
UNIVERSITY OF ILLINOIS AT URBANA-CHAMPAIGN

UNCLASSIFIED

SECURITY CLASSIFICATION OF THIS PAGE

REPORT DOCUMENTATION PAGE

Form Approved
OMB No. 0704-0188

1a. REPORT SECURITY CLASSIFICATION Unclassified	1b. RESTRICTIVE MARKINGS None
2a. SECURITY CLASSIFICATION AUTHORITY	3. DISTRIBUTION / AVAILABILITY OF REPORT Approved for public release; distribution unlimited
2b. DECLASSIFICATION / DOWNGRADING SCHEDULE	
4. PERFORMING ORGANIZATION REPORT NUMBER(S) UILU-ENG-90-2254	5. MONITORING ORGANIZATION REPORT NUMBER(S)
6a. NAME OF PERFORMING ORGANIZATION Coordinated Science Lab University of Illinois 6b. OFFICE SYMBOL (If applicable) N/A	7a. NAME OF MONITORING ORGANIZATION Office of Naval Research
6c. ADDRESS (City, State, and ZIP Code) 1101 W. Springfield Ave. Urbana, IL 61801	7b. ADDRESS (City, State, and ZIP Code) Arlington, VA 22217
8a. NAME OF FUNDING / SPONSORING ORGANIZATION Joint Services Electronics Program 8b. OFFICE SYMBOL (If applicable)	9. PROCUREMENT INSTRUMENT IDENTIFICATION NUMBER N00014-90-J-1270
8c. ADDRESS (City, State, and ZIP Code) Arlington, VA 22217	10. SOURCE OF FUNDING NUMBERS PROGRAM ELEMENT NO. / PROJECT NO. / TASK NO. / WORK UNIT ACCESSION NO.

11. TITLE (Include Security Classification)
Efficient Evaluation of the Inner Products in the Spectral Domain Analysis of Microstrip Discontinuities.

12. PERSONAL AUTHOR(S)
Dan McNay and Raj Mittra

13a. TYPE OF REPORT	13b. TIME COVERED	14. DATE OF REPORT (Year, Month, Day)	15. PAGE COUNT
Technical	FROM _____ TO _____	November 8, 1990	66

16. SUPPLEMENTARY NOTATION

17. COSATI CODES			18. SUBJECT TERMS (Continue on reverse if necessary and identify by block number)
FIELD	GROUP	SUB-GROUP	Microstrip Discontinuities; Method of Moments; Spectral Domain Approach; Asymptotic Evaluation of Integrals

19. ABSTRACT (Continue on reverse if necessary and identify by block number)

The current trend in microwave and millimeter-wave integrated circuits (MICs) is towards higher operating frequencies, high packing densities, and more stringent performance requirements. As a result, earlier models based on approximate analysis techniques are becoming insufficiently accurate for use in computer-aided design (CAD) packages. In particular, simplifying assumptions, such as the quasi-static approximation and the magnetic wall approximation, are becoming inappropriate in the analysis of microstrip discontinuities such as bends, steps, and stubs. Instead, a rigorous full-wave analysis is needed to obtain a more accurate characterization of these passive circuits. Such an analysis captures the increasingly significant effects of coupling, dispersion, and radiation. The objective of this study is to develop an asymptotic acceleration technique for the efficient evaluation of the integrals involved in the full-wave spectral domain method for analyzing microstrip discontinuity problems.

20. DISTRIBUTION / AVAILABILITY OF ABSTRACT ☒ UNCLASSIFIED/UNLIMITED ☐ SAME AS RPT. ☐ DTIC USERS	21. ABSTRACT SECURITY CLASSIFICATION Unclassified
22a. NAME OF RESPONSIBLE INDIVIDUAL	22b. TELEPHONE (Include Area Code) / 22c. OFFICE SYMBOL

DD Form 1473, JUN 86 *Previous editions are obsolete.*

SECURITY CLASSIFICATION OF THIS PAGE

UNCLASSIFIED

TABLE OF CONTENTS

CHAPTER 1
INTRODUCTION

The current trend in microwave and millimeter-wave integrated circuits (MICs) is towards higher operating frequencies, higher packing densities, and more stringent performance requirements. As a result, earlier models based on approximate analysis techniques are becoming insufficiently accurate for use in computer-aided design (CAD) packages. In particular, simplifying assumptions, such as the quasi-static approximation and the magnetic wall approximation, are becoming inappropriate in the analysis of microstrip discontinuities such as bends, steps, and stubs. Instead, a rigorous full-wave analysis is needed to obtain a more accurate characterization of these passive circuits. Such an analysis captures the increasingly significant effects of coupling, dispersion, and radiation.

One of the full-wave analysis techniques that has received considerable attention recently is the spectral domain approach. This is an integral equation approach that is solved numerically in the spectral domain by applying the method of moments. The open-end and gap discontinuities have been analyzed with this technique in [1] and [2], and the analysis of the step junction has been treated in [3]. In a recent work by Jackson [4], the analyses of the step, stub, and bent stub were presented.

Although the spectral domain approach has been successfully employed in a variety of problems, there is a definite need for improvement. This approach is computationally expensive for even the simplest geometries and quickly becomes intractable for larger problems. The primary source of difficulty is the evaluation of the inner products arising from the moment method. In the spectral domain approach, these inner products are two-dimensional integrals with infinite limits of integration. Since these integrals are too complicated to be evaluated analytically, we must resort to numerical techniques. Unfortunately, performing the integrations numerically is complicated by the fact that the

integrands will have one or more singularities and are often highly oscillatory. The most troubling and time-consuming aspect of these integrations, however, is the fact that the integrands decay quite slowly.

The major portion of this thesis is therefore devoted to the efficient evaluation of the inner products. In particular, an asymptotic acceleration technique is applied to the numerical integrations to enhance their rate of convergence. In this technique, the asymptotic form of the integrand is derived and then subtracted from the original integrand. The resulting integral will then converge more rapidly. In order to recover the original inner product , the asymptotic form is integrated separately and added back. An overall speedup in the computation is realized only if the asymptotic form can be integrated efficiently. In our work, the integral of the asymptotic form has been derived analytically in closed form. In this way, the maximal speedup from the asymptotic extraction is achieved, and more importantly, the technique is exact in the sense that no simplifying approximations were made.

In Chapter 2, the general microstrip discontinuity problem is formulated in the spectral domain. The moment method is then applied in Chapter 3, resulting in a system of equations with the inner products described above. In Chapter 4, the difficulties involved in the computation of these inner products is discussed in detail. In addition, symmetry relations are presented that allow a reduction in the range of integration. The asymptotic acceleration technique is presented in Chapter 5. In Chapter 6, comparisons are made between an algorithm that utilizes the acceleration technique and one that does not. Finally, conclusions and directions for future work are given in Chapter 7.

CHAPTER 2

THEORETICAL DEVELOPMENT

With the increase in the operating frequencies of microwave integrated circuits, previous models of passive circuits based on approximate analysis techniques are becoming insufficiently accurate. With this in mind, a full-wave analysis in the spectral domain is developed in this work to derive more accurate models for a variety of microstrip discontinuities. The analysis developed herein is rigorous, one that incorporates wave phenomena including radiation, dispersion, coupling, and surface wave propagation. In this approach, the microstrip discontinuity is characterized by solving for the reflection and transmission coefficients. From these coefficients, a suitable circuit model can be obtained for use in circuit simulation programs.

In this chapter, the conventional spatial domain analysis is presented first. The electric field is represented in terms of the currents on the microstrip through a dyadic Green's function. Since the Green's function is unavailable in closed form in the spatial domain, the formulation is continued in the spectral domain wherein the Green's function is known. After obtaining the general spectral domain equations, these equations are applied to the microstrip discontinuity.

The microstrip discontinuity is analyzed as a two-port network that is excited by a precomputed incident current density. This sinusoidally varying current is determined by solving for the fundamental mode on a uniform microstrip line. The forms of the reflected and transmitted currents on the input and output microstrip lines are also assumed to be the same as for the current on a uniform microstrip line. Therefore, the reflected and the transmitted currents are precomputed to within a multiplicative constant, namely, the reflection or transmission coefficient. In the process of solving for the unknown coefficients, the currents within the discontinuity are also obtained.

2.1 The Dyadic Green's Function

The open microstrip structure considered is shown in Fig. 2.1. (Figures and tables appear at the end of each chapter.) The conducting strip is located on a substrate of relative dielectric permittivity ε_r and of thickness d. In conventional spatial domain analysis, the electric field is represented in terms of the currents on a conducting body through a dyadic Green's function. Assuming time harmonic fields with the $e^{j\omega t}$ time convention, the electric field on the substrate can be represented as

$$\mathbf{E}(x,z) = \iint \overline{\overline{G}}(x-x',z-z')\,\mathbf{J}(x',z')\,dx'dz' \tag{2.1}$$

where $\mathbf{J}$ is the current density, and $\overline{\overline{G}}$ is the dyadic Green's function. The dyadic Green's function $\overline{\overline{G}}(x,z)$ represents the electric field at the point (x,z) due to an infinitesimal dipole of unit strength located at the origin. The integration in (2.1) is performed over the strip where the current exists.

When Equation (2.1) is enforced on the strip, the tangential electric field components E_x and E_z must be zero to satisfy the boundary condition. This leads to a set of coupled homogeneous integral equations

$$\begin{aligned}
&\iint [G_{xx}(x-x',z-z')J_x(x',z') \\
&\qquad + G_{xz}(x-x',z-z')J_z(x',z')]\,dx'dz' = 0 \\
&\iint [G_{zx}(x-x',z-z')J_x(x',z') \\
&\qquad + G_{zz}(x-x',z-z')J_z(x',z')]\,dx'dz' = 0
\end{aligned} \tag{2.2}$$

where the vector equation has been broken into its scalar components. If the Green's function were known in the spatial domain, Equation (2.2) could be used to solve for the

currents on the microstrip. Unfortunately, for the microstrip structure, a closed-form expression for the Green's function is not known.

A parallel analysis may be carried out in the spectral domain where the Green's function for a grounded dielectric slab can be obtained using a transmission line approach [5]. Taking the Fourier transform of (2.1) converts the convolution-type equations to the following algebraic equations

$$\begin{aligned} \tilde{G}_{xx}(\alpha,\beta)\tilde{J}_x(\alpha,\beta) + \tilde{G}_{xz}(\alpha,\beta)\tilde{J}_z(\alpha,\beta) &= \tilde{E}_x(\alpha,\beta) \\ \tilde{G}_{zx}(\alpha,\beta)\tilde{J}_x(\alpha,\beta) + \tilde{G}_{zz}(\alpha,\beta)\tilde{J}_z(\alpha,\beta) &= \tilde{E}_z(\alpha,\beta) \end{aligned} \tag{2.3}$$

where the tilde denotes the Fourier transform operator. The definition of the Fourier transform and its inverse transform have been taken to be

$$\tilde{f}(\alpha,\beta) = \int_{-\infty}^{\infty}\int_{-\infty}^{\infty} f(x,z)e^{-j(\alpha x+\beta z)}\,dxdz \tag{2.4}$$

and

$$f(x,z) = \frac{1}{(2\pi)^2}\int_{-\infty}^{\infty}\int_{-\infty}^{\infty} \tilde{f}(\alpha,\beta)e^{j(\alpha x+\beta z)}\,d\alpha d\beta\,, \tag{2.5}$$

respectively.

Note that Equation (2.1) was transformed instead of Equation (2.2). This is necessary since the transform is taken over the entire spatial domain and (2.2) is defined only on the strip. As a result, the transform of the electric field in (2.3) is nonzero. This electric field is unknown, but can be eliminated when the moment method is applied (this is discussed further in Chapter 3).

The spectral domain Green's function for the open microstrip structure is derived in detail by Itoh and Menzel [6]; therefore, only the result is presented here. In the derivation, the strip is considered to be infinitesimally thin, and both the ground plane and the strip are

treated as perfect electric conductors. An equivalent, more compact form of the Green's function is given by [7]

$$\tilde{G}_{xx}(\alpha,\beta) = \frac{\alpha^2 D_3 - k_o^2 D_1}{\omega\varepsilon_o D_1 D_2} \tag{2.6}$$

$$\tilde{G}_{xz}(\alpha,\beta) = \frac{\alpha\beta D_3}{\omega\varepsilon_o D_1 D_2} \tag{2.7}$$

$$\tilde{G}_{zx}(\alpha,\beta) = \tilde{G}_{xz}(\alpha,\beta) \tag{2.8}$$

$$\tilde{G}_{zz}(\alpha,\beta) = \frac{\beta^2 D_3 - k_o^2 D_1}{\omega\varepsilon_o D_1 D_2} \tag{2.9}$$

where

$$k_o = \frac{2\pi}{\lambda_o}$$

$$s = \sqrt{k_o^2 - \alpha^2 - \beta^2}$$

$$s' = \sqrt{\varepsilon_r k_o^2 - \alpha^2 - \beta^2}$$

$$D_1 = s' - js\varepsilon_r \cot(s'd)$$

$$D_2 = s - js' \cot(s'd)$$

$$D_3 = s' - js\cot(s'd)$$

and where the positive real or negative imaginary root is taken in the evaluation of s and s´.

2.2 Spectral Equations Describing the Microstrip Discontinuity

The geometry of a general microstrip discontinuity is shown in Fig. 2.2, where the particular discontinuity is defined within a discrete mesh region. The discontinuity is analyzed as a two-port network where the reference planes are defined at z=0 and z=L. The network is excited at z=0 by an incident current density which is assumed to have the same form as the current density on a uniform microstrip line. The reference planes are

assumed to be sufficiently far from the discontinuity so that the reflected and the transmitted currents can be approximated by currents on a uniform microstrip line. The currents within the mesh region are entirely unknown. The spectral current density appearing in Equation (2.3) is then the superposition of the boundary currents and the mesh region currents, given by

$$\tilde{\mathbf{J}}(\alpha,\beta) = \tilde{\mathbf{J}}^{I}(\alpha,\beta) + \Gamma\tilde{\mathbf{J}}^{R}(\alpha,\beta) + T\tilde{\mathbf{J}}^{T}(\alpha,\beta) + \tilde{\mathbf{J}}^{mr}(\alpha,\beta) \tag{2.10}$$

where $\mathbf{J}^{I}$ is the incident current density, $\mathbf{J}^{R}$ and $\mathbf{J}^{T}$ are the reflected and transmitted currents, and $\mathbf{J}^{mr}$ is the unknown current density within the mesh region. The reflection and transmission coefficients are given by Γ and T, respectively.

The boundary current densities in (2.10) may be represented in the spatial domain as

$$\mathbf{J}^{I}(x,z) = \left[\hat{\mathbf{x}}\, f_{x1}(x,z) + \hat{\mathbf{z}}\, f_{z1}(x,z)\right] e^{-j\beta_{o1}z} \tag{2.11}$$

$$\mathbf{J}^{R}(x,z) = \left[-\hat{\mathbf{x}}\, f_{x1}(x,z) + \hat{\mathbf{z}}\, f_{z1}(x,z)\right] e^{+j\beta_{o1}z} \tag{2.12}$$

$$\mathbf{J}^{T}(x,z) = \left[\hat{\mathbf{x}}\, f_{x2}(x,z) + \hat{\mathbf{z}}\, f_{z2}(x,z)\right] e^{-j\beta_{o2}z} \tag{2.13}$$

where the functions f_{x1},f_{z1},f_{x2}, and f_{z2} represent the transverse distribution of currents, and β_{o1} and β_{o2} are the propagation constants. The propagation constants and the transverse distributions are precomputed by solving for the fundamental mode of a uniform microstrip line [5]. Specifically, Equation (2.3) is solved numerically for the case in which the microstrip is invariant in the z-direction and there is no source excitation. The numerical technique is essentially a simplification of the technique to be described in Chapter 3.

The only remaining unknowns in (2.10) are $\tilde{\mathbf{J}}^{mr}$, Γ and T. These are found by solving (2.3). Substitution of (2.10) into (2.3) yields

$$\begin{aligned}
\tilde{G}_{xx}\tilde{J}_x^{mr} + \tilde{G}_{xz}\tilde{J}_z^{mr} + \Gamma\left(\tilde{G}_{xx}\tilde{J}_x^{R} + \tilde{G}_{xz}\tilde{J}_z^{R}\right) + T\left(\tilde{G}_{xx}\tilde{J}_x^{T} + \tilde{G}_{xz}\tilde{J}_z^{T}\right) &= \tilde{E}_x - \left(\tilde{G}_{xx}\tilde{J}_x^{I} + \tilde{G}_{xz}\tilde{J}_z^{I}\right) \\
\tilde{G}_{zx}\tilde{J}_x^{mr} + \tilde{G}_{zz}\tilde{J}_z^{mr} + \Gamma\left(\tilde{G}_{zx}\tilde{J}_x^{R} + \tilde{G}_{zz}\tilde{J}_z^{R}\right) + T\left(\tilde{G}_{zx}\tilde{J}_x^{T} + \tilde{G}_{zz}\tilde{J}_z^{T}\right) &= \tilde{E}_z - \left(\tilde{G}_{zx}\tilde{J}_x^{I} + \tilde{G}_{zz}\tilde{J}_z^{I}\right)
\end{aligned} \tag{2.14}$$

where for simplicity the arguments of the functions have been dropped. The numerical solution of (2.14) is discussed in Chapter 3.

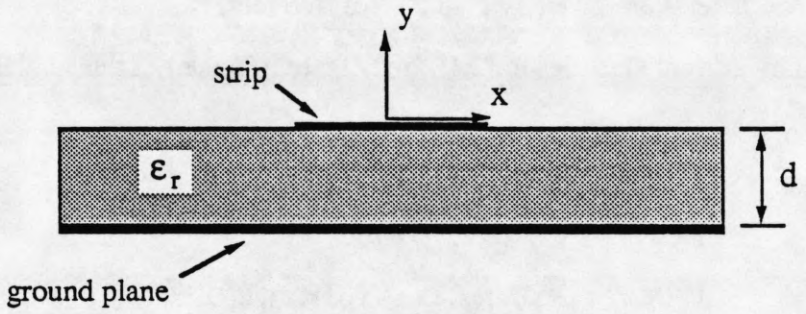

Figure 2.1. Cross section of an open microstrip line.

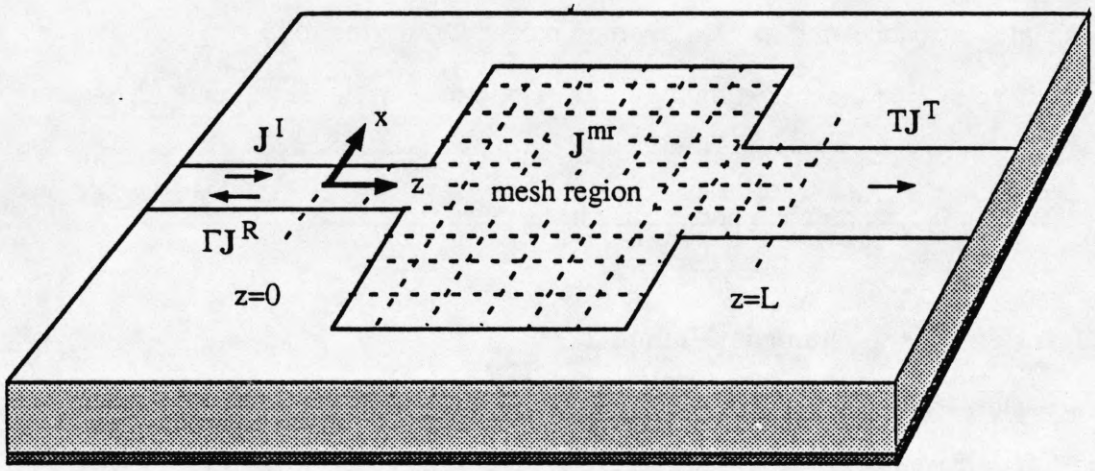

Figure 2.2. Geometry of a general microstrip discontinuity.

CHAPTER 3

NUMERICAL PROCEDURE

In Chapter 2, the general microstrip discontinuity problem was formulated in the spectral domain, and the electric field was represented in terms of the current densities on the strip. In this chapter, the moment method is applied to the spectral domain Equation (2.14) to generate a system of equations that can be solved numerically. The first section of this chapter introduces the moment method procedure. In the following section, the procedure is applied to the discontinuity problem, and the current densities in (2.14) are expanded in terms of basis functions. The final section provides the criteria for selecting a suitable set of basis functions and presents the basis functions used in this work.

3.1 Overview of the Moment Method

The moment method is a mathematical technique used to reduce functional equations to matrix equations [8]. Consider the linear equation

$$L(f) = s \tag{3.1}$$

In this equation, L is a linear operator, s represents a source, and f is an unknown function such as a field or current. The problem is to determine the function f when the inverse linear operator L^{-1} is unknown.

The function f is first expanded into a series of basis functions $f_1, f_2, \ldots, f_N$ defined over the domain of L

$$f = \sum_{i=1}^{N} a_i f_i \tag{3.2}$$

The basis functions should be linearly independent and chosen so that a weighted sum of these functions can represent f reasonably well. Depending on the choice of basis functions, the series representation will be approximate or exact . The basis functions used in this work are subsectional basis functions where each f_i is defined over only a subsection of the domain of f. In this case, Equation (3.2) will most likely be an approximate representation of f, given a finite N.

Equation (3.2) is then substituted into the linear Equation (3.1) to give

$$\sum_{i=1}^{N} a_i L(f_i) = s \tag{3.3}$$

A set of N equations is needed to solve for the unknown coefficients a_i. These equations are obtained by choosing N weighting or testing functions $w_1, w_2, \ldots, w_N$ and taking a suitable inner product of (3.3) with each testing function. When the basis and testing functions are the same, the procedure is known as Galerkin's method. The final set of equations is expressed in matrix form as

$$\begin{bmatrix} \langle w_1, L(f_1)\rangle & \langle w_1, L(f_2)\rangle & \cdots & \langle w_1, L(f_N)\rangle \\ \langle w_2, L(f_1)\rangle & \langle w_2, L(f_2)\rangle & \cdots & \langle w_2, L(f_N)\rangle \\ \vdots & \vdots & \ddots & \vdots \\ \langle w_N, L(f_1)\rangle & \langle w_N, L(f_2)\rangle & \cdots & \langle w_N, L(f_N)\rangle \end{bmatrix} \begin{bmatrix} a_1 \\ a_2 \\ \vdots \\ a_N \end{bmatrix} = \begin{bmatrix} \langle w_1, s\rangle \\ \langle w_2, s\rangle \\ \vdots \\ \langle w_N, s\rangle \end{bmatrix} \tag{3.4}$$

These equations can be solved numerically using a number of techniques. Since the limiting factor in this method is the computation time required to evaluate the inner products, the size of the matrix in (3.4) must be kept small. Consequently, the matrix inversion is not a problem.

3.2 Application of the Moment Method to the Microstrip Discontinuity

The moment method is now applied to the spectral domain Equation (2.14) describing the microstrip problem. Here, the Green's function is the linear operator and the unknown function is the current density in the discontinuity region. Two additional unknowns are the reflection and transmission coefficients Γ and T. The source function is the incident current density $\mathbf{J}^I$.

To apply the moment method, the spectral current densities in the mesh region are first expanded in terms of basis functions

$$\begin{aligned} \tilde{J}_x^{mr}(\alpha,\beta) &= \sum_{i=1}^{N} a_i \tilde{J}_{xi}(\alpha,\beta) \\ \tilde{J}_z^{mr}(\alpha,\beta) &= \sum_{i=1}^{M} b_i \tilde{J}_{zi}(\alpha,\beta) \end{aligned} \tag{3.5}$$

where a_i and b_i are the weight coefficients and $\tilde{J}_{xi}$ and $\tilde{J}_{zi}$ are the basis functions. The boundary currents $\mathbf{J}^I$, $\mathbf{J}^R$, and $\mathbf{J}^T$ are also expanded in terms of basis functions such that

$$\begin{aligned} \tilde{J}_x^Q(\alpha,\beta) &= \sum_i c_i^Q \tilde{J}_{xi}^Q(\alpha,\beta) \\ \tilde{J}_z^Q(\alpha,\beta) &= \sum_i d_i^Q \tilde{J}_{zi}^Q(\alpha,\beta) \end{aligned} \tag{3.6}$$

where

$$Q = I, R, \text{ or } T$$

All of the constants c_i^Q and d_i^Q are known, since the boundary currents are precomputed. The boundary current densities are actually represented in terms of basis functions for reasons that are not associated with the moment method. The main reason is that the transverse current distribution is calculated numerically and therefore must be

approximated. Also, the boundary currents are semiinfinite, but they are truncated to simplify the computation.

The current expansions (3.5) and (3.6) are then substituted into (2.14), and the inner product of this equation is taken with testing functions. The inner product definition adopted in this work is

$$\langle f(\alpha,\beta), g(\alpha,\beta)\rangle = \int_{-\infty}^{\infty}\int_{-\infty}^{\infty} f^{*}(\alpha,\beta)\, g(\alpha,\beta)\, d\alpha d\beta \tag{3.7}$$

where the function f is the testing function, and the function g is the Green's function multiplied by a current basis function. Physically this type of testing will give the integrated electric field over the area of the testing function due to a current element radiating over the grounded dielectric slab.

The testing procedure is almost Galerkin. The first row in (2.14) is tested N times with $\tilde{J}_{xi}(\alpha,\beta)$, and the second row is tested M times with $\tilde{J}_{zi}(\alpha,\beta)$. However, this will yield only (N+M) equations to solve for the (N+M+2) unknowns. The last two equations are obtained by testing at the junctions between the mesh region and the input and output reference planes. Since the z-directed current will be dominant, the inner product testing is taken with the second row of (2.14). The boundary testing functions are denoted as $\tilde{W}_1(\alpha,\beta)$ and $\tilde{W}_2(\alpha,\beta)$. The final matrix form is then

$$\left[\begin{array}{cc:cc} Z_{xx} & Z_{xz} & Z_{xR} & Z_{xT} \\ Z_{zx} & Z_{zz} & Z_{zR} & Z_{zT} \\ \hdashline Z_{w1x} & Z_{w1z} & Z_{w1R} & Z_{w1T} \\ Z_{w2x} & Z_{w2z} & Z_{w2R} & Z_{w2T} \end{array}\right] \left[\begin{array}{c} a_i \\ b_i \\ \Gamma \\ T \end{array}\right] = -\left[\begin{array}{c} V_{xI} \\ V_{zI} \\ V_{wII} \\ V_{w2I} \end{array}\right] \tag{3.8}$$

where the matrix elements shown are submatrices.

The upper left block of submatrices in (3.8) results from the testing between basis functions within the mesh region. These are the largest submatrices and increase in size as the square of the number of basis functions. The upper right block consists of inner products where the testing is between the mesh region basis functions and the reflected or transmitted currents. Each of these submatrices are column vectors. The last two rows in (3.8) are the two additional equations needed to solve for Γ and T. Finally, the vector on the right-hand side results from taking the inner product between each of the testing functions and the incident current.

The similarities between different submatrices are readily seen when the submatrices are written in compact form. The general term in each submatrix is given by

$$(Z_{pq})_{ji} = \left\langle \tilde{J}_{pj}, \tilde{G}_{pq}\tilde{J}_{qi} \right\rangle \qquad \text{(matrix)}$$

$$(Z_{pQ})_{j} = \left\langle \tilde{J}_{pj}, \left(\tilde{G}_{px}\tilde{J}_{x}^{Q} + \tilde{G}_{pz}\tilde{J}_{z}^{Q}\right) \right\rangle \qquad \text{(column vector)}$$

$$(Z_{wnq})_{i} = \left\langle \tilde{W}_{n}, \tilde{G}_{zq}\tilde{J}_{qi} \right\rangle \qquad \text{(row vector)}$$

$$(Z_{wnQ}) = \left\langle \tilde{W}_{n}, \left(\tilde{G}_{px}\tilde{J}_{x}^{Q} + \tilde{G}_{pz}\tilde{J}_{z}^{Q}\right) \right\rangle \qquad \text{(scalar)}$$

$$(V_{pI})_{j} = \left\langle \tilde{J}_{pj}, \left(\tilde{G}_{px}\tilde{J}_{x}^{I} + \tilde{G}_{pz}\tilde{J}_{z}^{I}\right) \right\rangle \qquad \text{(column vector)}$$

$$(V_{wnI}) = \left\langle \tilde{W}_{n}, \left(\tilde{G}_{zx}\tilde{J}_{x}^{I} + \tilde{G}_{zz}\tilde{J}_{z}^{I}\right) \right\rangle \qquad \text{(scalar)}$$

where

$p = x \text{ or } z$
$q = x \text{ or } z$
$Q = R \text{ or } T$
$n = 1 \text{ or } 2$

Note that the unknown electric field in the right-hand side of (2.14) was eliminated in the testing process and does not appear in the blocks V_{pI} or V_{wnI}. This is explained by applying Parseval's theorem to the inner products. As an example, consider the inner

product $\langle \tilde{J}_{xj}, \tilde{G}_{xx}\tilde{J}_{xi} \rangle$, which is equivalent to $\langle \tilde{J}_{xj}, \tilde{E}_x \rangle$. After applying Parseval's theorem, the inner product becomes

$$\begin{aligned} \left\langle \tilde{J}_{xj}, \tilde{G}_{xx}\tilde{J}_{xi} \right\rangle &= \int_{-\infty}^{\infty}\int_{-\infty}^{\infty} \tilde{J}^{*}_{xj}(\alpha,\beta)\tilde{E}_x(\alpha,\beta)\, d\alpha d\beta \\ &= 4\pi^2 \int_{-\infty}^{\infty}\int_{-\infty}^{\infty} J_{xj}(x,z)E_x(x,z)\, dxdz \\ &= 0 \end{aligned} \tag{3.9}$$

The inner product is zero, because in the spatial domain the current density and the electric field on the substrate are zero in complementary regions. For instance, the current is zero everywhere except on the conducting strip where the electric field is zero. Therefore, the integrand in the second integral is identically zero.

3.3 Basis Functions

As mentioned in Section 3.1, the choice of basis functions can affect the accuracy of the current representation. A good choice can also reduce the number of basis functions needed to obtain adequate results. When choosing basis functions, there are several issues that must be considered. These are the geometry of the problem, the current behavior, and the inner product evaluation.

The geometry of the problem will dictate the use of either entire domain or subdomain basis functions. In this work, subdomain basis functions are used so that a variety of microstrip discontinuities may be analyzed. The geometry of the discontinuity is actually defined by the location of the current basis functions, since the basis functions are placed only on the conducting strip where current exists. For complicated geometries, the subdomain basis functions also offer the advantage that no prior knowledge of the current behavior is needed. This is contrasted with the patch antenna problem where entire domain

basis functions may be used, because the geometry is fixed and there is some knowledge of the modal distribution of current.

In order to model the currents efficiently, some important aspects of the current behavior should be built into the basis functions. One such characteristic is the well-known edge condition. This refers to the fact that for current traveling along an edge, the current distribution will tend towards infinity near the edge. Another characteristic is that currents traveling towards an edge of a conductor should go to zero by current continuity. The basis functions are chosen to exhibit these properties.

The final consideration in choosing the basis functions is to ensure that the integration in the inner product evaluation is convergent. A careful look at Equations (2.6)-(2.9) will show that the Green's function increases without bound for large α and β. If the two-dimensional integration is converted into polar coordinates by making the substitutions $\alpha=\rho\sin\theta$ and $\beta=\rho\cos\theta$, it can be shown that for large ρ the components of the asymptotic Green's function tend to $\tilde{G}_{xx} \approx \rho\sin^2\theta$, $\tilde{G}_{xz} \approx \rho\sin\theta\cos\theta$, and $\tilde{G}_{zz} \approx \rho\cos^2\theta$. Since the coordinate transformation introduces another ρ as a metric coefficient, the spectral domain basis and testing functions must introduce a factor of at least ρ^{-p}, $p>3$, to guarantee convergence.

In the spatial domain, the "rooftop" expansion functions depicted in Fig. 3.1 are used as basis functions in the mesh region. These basis functions are composed of a triangle function in the direction of current flow and a pulse function in the other direction. The pulse and triangle functions are defined as

$$\Pi_T(t) = \begin{cases} 1, & |t| \le \dfrac{T}{2} \\ 0, & |t| > \dfrac{T}{2} \end{cases} \tag{3.10}$$

$$\Lambda_w(t) = \begin{cases} 1 - \dfrac{|t|}{w}, & |t| \le w \\ 0, & |t| > w \end{cases} \tag{3.11}$$

where the corresponding Fourier transforms with respect to the spectral variable ω are

$$\tilde{\Pi}_T(\omega) = T\frac{\sin(\omega T/2)}{(\omega T/2)} \tag{3.12}$$

$$\tilde{\Lambda}_w(\omega) = w\left[\frac{\sin(\omega w/2)}{(\omega w/2)}\right]^2 \tag{3.13}$$

Combining these two functions in the spatial domain, the mesh region basis functions for the x and z-directed currents become

$$J_{xi}(x,z) = \Lambda_{w_x}(x - x_i)\Pi_{t_x}(z - z_i) \tag{3.14}$$

$$J_{zi}(x,z) = \Pi_{t_z}(x - x_i)\Lambda_{w_z}(z - z_i) \tag{3.15}$$

For each component of current, the widths and thicknesses of all the "rooftop" basis functions are assumed to be equal. The center of the ith basis function is (x_i,z_i), and the basis functions are positioned so that the triangle functions of neighboring "rooftops" overlap and the pulse functions are edge to edge. The current represented by these basis functions goes to zero in the direction of current flow, and the basis functions are suited to model the edge condition.

The spectral domain basis functions are obtained by taking the Fourier transform of (3.14) and (3.15)

$$\tilde{J}_{xi}(\alpha,\beta) = \tilde{\Lambda}_{w_x}(\alpha)\tilde{\Pi}_{t_x}(\beta)\, e^{-j(\alpha x_i + \beta z_i)} \tag{3.16}$$

$$\tilde{J}_{zi}(\alpha,\beta) = \tilde{\Pi}_{t_z}(\alpha)\tilde{\Lambda}_{w_z}(\beta)\, e^{-j(\alpha x_i + \beta z_i)} \tag{3.17}$$

Each of these basis functions introduces a ρ^{-3} term in polar coordinates; therefore, the inner product integrals are convergent when the testing procedure is Galerkin.

The boundary currents are modeled in a manner consistent with the mesh region basis functions. The transverse current distribution is approximated as a weighted sum of pulse functions for the z-directed currents and triangle functions for the x-directed currents. The weighting coefficients are found by sampling the precomputed current distribution at the center of each basis function. The x-directed current is truncated at the mesh region as a pulse function while the z-directed current terminates in the mesh region as a triangle function. These basis functions are multiplied by the propagation factor $e^{\mp j\beta_{o}z}$ and are truncated at a distance t_b from the mesh. The boundary currents in the spatial domain are represented as

$$\begin{aligned} J_x^Q(x,z) &= \sum_i c_i^Q \Lambda_{w_x}(x-x_i)\Pi_{t_b}(z+t_b/2)\, e^{\mp j\beta_{o1}z} \\ J_z^Q(x,z) &= \sum_i d_i^Q \Pi_{t_z}(x-x_i)P(z+t_b/2)\, e^{\mp j\beta_{o1}z} \end{aligned} \tag{3.18}$$

$$\begin{aligned} J_x^T(x,z) &= \sum_i c_i^T \Lambda_{w_x}(x-x_i)\Pi_{t_b}(z-L-t_b/2)\, e^{-j\beta_{o2}z} \\ J_z^T(x,z) &= \sum_i d_i^T \Pi_{t_z}(x-x_i)P(z-L-t_b/2)\, e^{-j\beta_{o2}z} \end{aligned} \tag{3.19}$$

where

$$Q = I \text{ or } R$$

and where

$$P(t) = \begin{cases} \dfrac{1}{w_z}\left[(t_b/2+w_z)-|t|\right], & t_b/2 \le |t| < (t_b/2+w_z) \\ 1, & |t| \le t_b/2 \end{cases}$$

In (3.18) the negative sign is taken for the incident current and the positive sign for the reflected current. Figures 3.2-3.5 illustrate how the input boundary currents J^I and J^R are represented in terms of these basis functions.

The boundary testing functions are also chosen to be compatible with both the mesh region basis functions and the boundary current basis functions. These testing functions are a weighted sum of z-directed "rooftop" basis functions, where the weights are chosen to be consistent with the z-directed boundary currents. The testing function W_1 straddles the z=0 reference plane at the junction between the mesh region and the boundary currents. Similarly, the testing function W_2 straddles the reference plane at z=L. These boundary testing functions are represented in the spatial domain as

$$W_1(x,z) = \sum_i d_i^I \Pi_{t_z}(x - x_i) \Lambda_{w_z}(z) \tag{3.20}$$

$$W_2(x,z) = \sum_i d_i^T \Pi_{t_z}(x - x_i) \Lambda_{w_z}(z - L) \tag{3.21}$$

Finally, the basis and testing functions presented in this section are combined with the moment method procedure in Section 3.2 to construct the set of Equations (3.8). The numerical evaluation of the inner products is discussed next in Chapter 4.

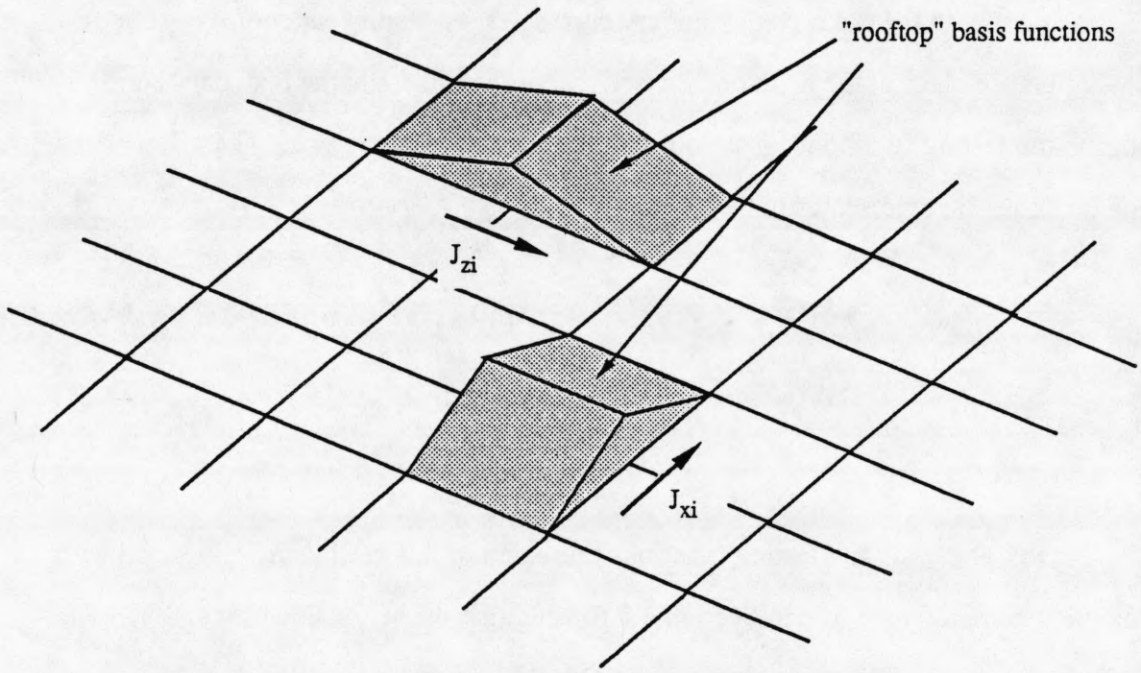

Figure 3.1. Illustration of "rooftop" basis functions in the mesh region.

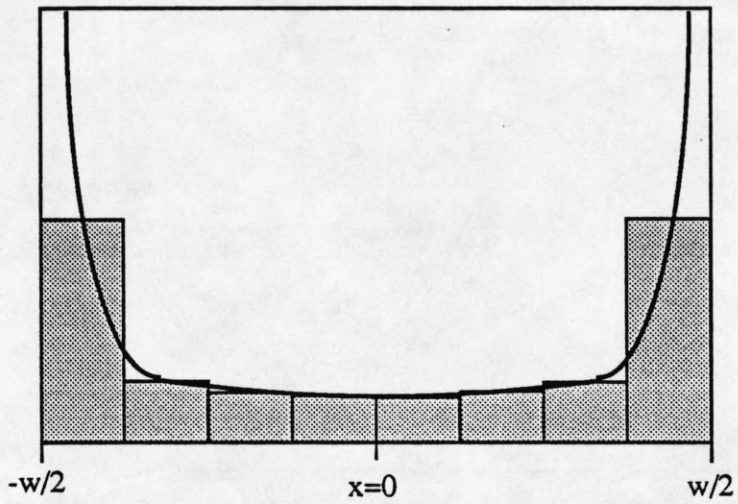

Figure 3.2. Transverse distribution of z-directed boundary currents represented by 8 basis functions.

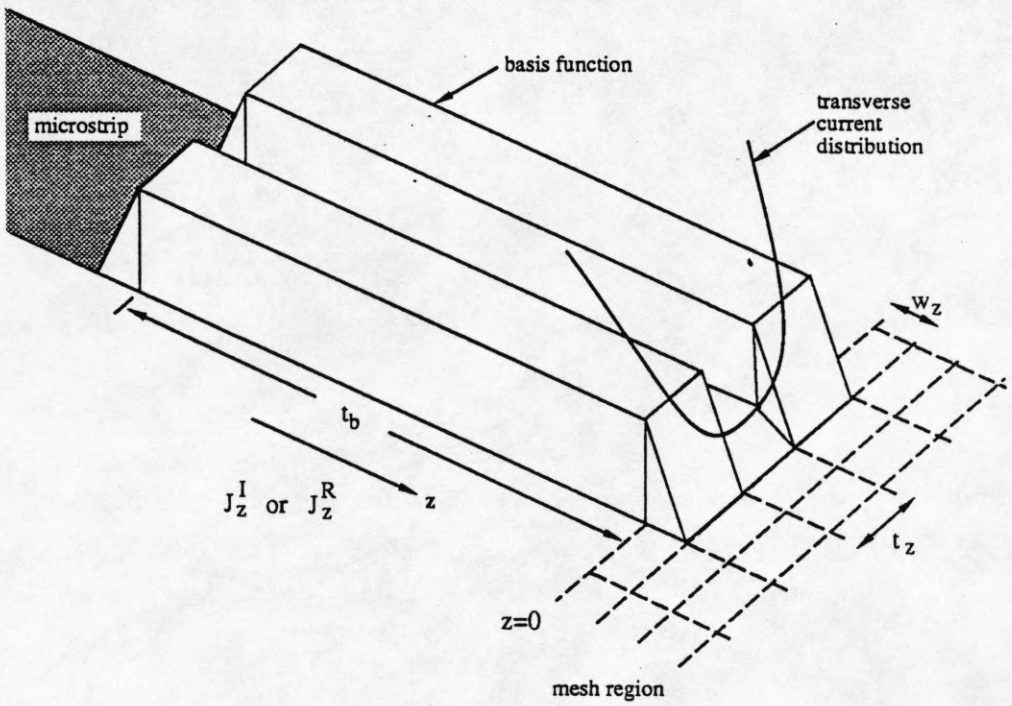

Figure 3.3. Representation of J_z^I or J_z^R with 3 basis functions.

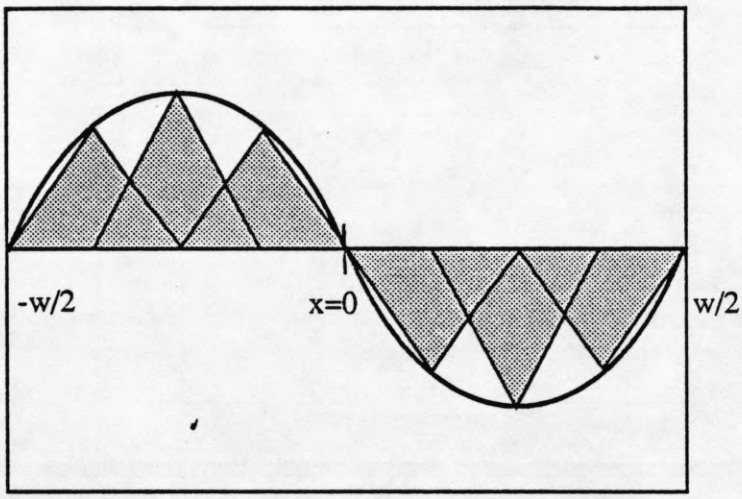

Figure 3.4. Transverse distribution of x-directed boundary currents represented by 7 basis functions.

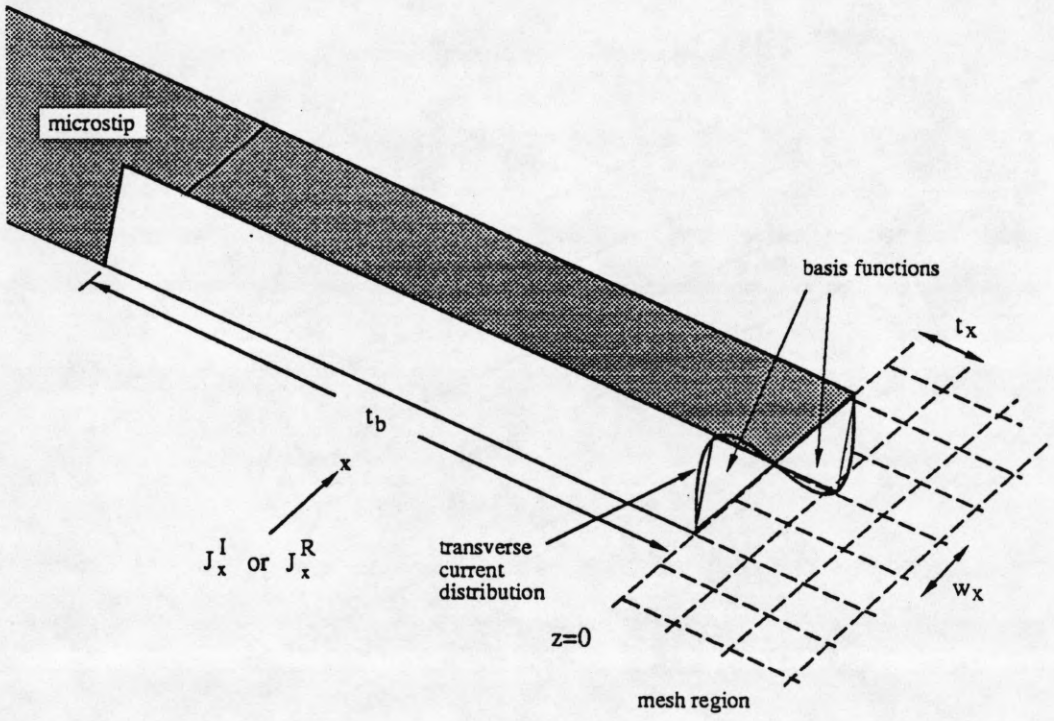

Figure 3.5. Representation of J_x^I or J_x^R with 3 basis functions.

CHAPTER 4

INNER PRODUCT EVALUATION

The formulation of the microstrip discontinuity problem is quite elegant and simple; implementing the numerical procedure is considerably more difficult. At first glance, constructing the set of matrix equations in (3.8) appears relatively straightforward. The only requirement is to compute the inner products between a testing function and the Green's function multiplied by a basis function. However, it is the evaluation of these inner products that is the primary source of difficulty in applying this method.

There are certain problems associated with the inner product evaluation that are apparent immediately. For instance, the required integrals are too complicated to be evaluated analytically; therefore, the integrations must be performed numerically. These integrals are doubly infinite which creates an additional problem. Since the infinite integrations must eventually be truncated, the rate of convergence is extremely important. Another problem is that the Green's function introduces singularities in the integrand, further complicating the integration.

With these problems in mind, an algorithm was developed to perform the analysis described in Chapters 2 and 3. This program was written to construct the matrix equations in (3.8) efficiently. All of the inner products were computed in parallel, reducing the number of times the functions were evaluated. Essentially, the program integrated the entire matrix and column vector in (3.8) at the same time. In the algorithm, the convergence problem was handled by choosing higher-order basis functions than those described in Chapter 3 in order to increase the rate of decay in the spectral domain. After running the program, it was found that the rate of convergence was insufficient. It was also discovered that the singularity in the integrand was treated unsuccessfully by adding loss to the permittivity of the dielectric substrate.

These findings warrant a more careful look into the evaluation of the inner products. Since the sizes of the four upper left blocks in (3.8) increase as the number of basis functions squared, these inner products are considered in particular. In this chapter, the symmetry in the integrand is examined and exploited to reduce the overall computation time. Then the nature of the singularities and possible methods to integrate them accurately are discussed. Finally, the convergence rate of the inner product integrals is discussed.

4.1 Symmetry in the Integrands

Since the number of inner products that need to be evaluated in a particular problem may become large, it is important to study methods to compute the inner product integrals more efficiently. If the symmetry in the integrands is taken into account, the numerical computation time of each inner product can be reduced by a factor of 4. This is accomplished by changing the limits of integration from the entire (α,β) plane to only the first quadrant. In this work, the numerical integrations are actually performed in the polar coordinate system, since the doubly infinite limits are then reduced to an infinite limit on only the ρ variable.

Although the integrations are performed in polar coordinates, it is easier to investigate the symmetry of the integrand in the Cartesian coordinate system. The symmetry of each function in the integrand is first analyzed, and then the entire integrand is considered. The Green's function (2.6)-(2.9) exhibits the following symmetry:

$$\begin{aligned}
&\tilde{G}_{xx}(\alpha,\beta) = \tilde{G}_{xx}(-\alpha,\beta) = \tilde{G}_{xx}(-\alpha,-\beta) = \tilde{G}_{xx}(\alpha,-\beta) \\
&\tilde{G}_{xz}(\alpha,\beta) = -\tilde{G}_{xz}(-\alpha,\beta) = \tilde{G}_{xz}(-\alpha,-\beta) = -\tilde{G}_{xz}(\alpha,-\beta) \\
&\tilde{G}_{zz}(\alpha,\beta) = \tilde{G}_{zz}(-\alpha,\beta) = \tilde{G}_{zz}(-\alpha,-\beta) = \tilde{G}_{zz}(\alpha,-\beta)
\end{aligned} \tag{4.1}$$

The components $\tilde{G}_{xx}$ and $\tilde{G}_{zz}$ are symmetric in all four quadrants, while $\tilde{G}_{xz}$ is asymmetric in the 2nd and 4th quadrants.

The symmetry of the basis and testing functions is determined by examining each function in Equations (3.16) and (3.17). The triangle and pulse functions are even functions with respect to α and β. The function that complicates the symmetry is the complex exponential that results from the shift of the basis functions from the origin in the spatial domain. For simplicity, the exponentials from the testing function and the basis function are grouped together and denoted by

$$Z(\alpha,\beta) = e^{-j(\alpha x' + \beta z')} \tag{4.2}$$

where

$$x' = (x_i - x_j)$$
$$z' = (z_i - z_j)$$

The location of the testing function, or field point, is (x_j,z_j) and the location of the current basis function, or source point, is (x_i,z_i). Note that the change of sign on the x_j and z_j of the testing function results from the conjugation in the inner product definition. The complex exponential function has the following symmetry

$$\begin{aligned} Z(-\alpha,-\beta) &= Z^*(\alpha,\beta) \\ Z(\alpha,-\beta) &= Z^*(-\alpha,\beta) \end{aligned} \tag{4.3}$$

Using the symmetries in (4.1) and (4.3), the inner product $\langle \tilde{J}_{xj}, \tilde{G}_{xx} \tilde{J}_{xi} \rangle$ can be written as

$$\left\langle \tilde{J}_{xj}, \tilde{G}_{xx} \tilde{J}_{xi} \right\rangle = \int_0^\infty \int_0^\infty \left\{ \tilde{\Lambda}^2_{w_x}(\alpha) \tilde{\Pi}^2_{t_x}(\beta) \tilde{G}_{xx}(\alpha,\beta) \left[Z(\alpha,\beta) + Z^*(\alpha,\beta) + Z(-\alpha,\beta) + Z^*(-\alpha,\beta) \right] \right\} d\alpha\, d\beta \tag{4.4}$$

where the integration is now over only the first quadrant. Each of the exponential terms corresponds to one quadrant in the (α,β) plane. These terms can be combined by grouping complex conjugate pairs to obtain twice the real part. The resulting cosine functions are then combined using a trigonometric identity. The final form of the inner product is then

$$\left\langle \tilde{J}_{xj}, \tilde{G}_{xx} \tilde{J}_{xi} \right\rangle = 4 \int_0^\infty \int_0^\infty \tilde{\Lambda}^2_{w_x}(\alpha) \tilde{\Pi}^2_{t_x}(\beta) \tilde{G}_{xx}(\alpha,\beta) \cos(\alpha x') \cos(\beta z') \, d\alpha \, d\beta \qquad (4.5)$$

The limits of integration for the other inner products are reduced to one quadrant in a similar fashion and are given by

$$\left\langle \tilde{J}_{xj}, \tilde{G}_{xz} \tilde{J}_{zi} \right\rangle = -4 \int_0^\infty \int_0^\infty \tilde{\Lambda}_{w_x}(\alpha) \tilde{\Pi}_{t_x}(\beta) \tilde{\Pi}_{t_z}(\alpha) \tilde{\Lambda}_{w_z}(\beta) \times \tilde{G}_{xz}(\alpha,\beta) \sin(\alpha x') \sin(\beta z') \, d\alpha \, d\beta \qquad (4.6)$$

$$\left\langle \tilde{J}_{zj}, \tilde{G}_{zz} \tilde{J}_{zi} \right\rangle = 4 \int_0^\infty \int_0^\infty \tilde{\Pi}^2_{t_z}(\alpha) \tilde{\Lambda}^2_{w_z}(\beta) \tilde{G}_{zz}(\alpha,\beta) \cos(\alpha x') \cos(\beta z') \, d\alpha \, d\beta \qquad (4.7)$$

Since the components $\tilde{G}_{xz}$ and $\tilde{G}_{zx}$ of the Green's function are identical, the inner product $\langle \tilde{J}_{zj}, \tilde{G}_{zx} \tilde{J}_{xi} \rangle$ is also given by Equation (4.7).

As previously mentioned, all of the numerical integrations are performed in polar coordinates. In this case, the limits of the integration are $(0,\pi/2)$ in θ and $(0,\infty)$ in ρ. One final observation is that when x' or z' is zero in Equation (4.7), the inner product is identically zero. This agrees with the physical intuition gained from studying a dipole radiating in free space. For instance, a z-directed dipole located at the origin will produce a radiation pattern that has no x-directed electric field along either the x-axis or the z-axis. This property apparently remains true for a dipole radiating over a grounded dielectric slab.

4.2 Singularities

One of the major difficulties in the evaluation of the inner products is the numerical integration of the singularities. The singularities in the integrand are introduced by the terms D_1 and D_2 in the denominator of the Green's function (2.6)-(2.9). Each of the poles of the Green's function corresponds to a resonance condition, namely, a source-free solution to Maxwell's equations for the grounded dielectric slab. Physically, the zeros of D_1 and D_2 represent the TM and TE surface wave poles, respectively.

These surface wave poles are determined by solving for the roots of the equations

$$s - js'\cot(s'd) = 0 \qquad \text{(TE)} \tag{4.8}$$

$$s' - js\varepsilon_r \cot(s'd) = 0 \qquad \text{(TM)} \tag{4.9}$$

where

$$s = \sqrt{k_o^2 - \rho^2}$$

$$s' = \sqrt{\varepsilon_r k_o^2 - \rho^2}$$

These equations are functions of only the variable ρ in polar coordinates, and therefore the singularities are encountered only in the ρ integration.

A careful examination of Equations (4.8) and (4.9) will show that in the case of a lossless dielectric (ε_r real), the singularities occur for real values of ρ in the region $k_o<\rho<\sqrt{\varepsilon_r}k_o$. The number of singularities within this region can be shown to be [9]

$$N_{TE} = \begin{cases} 0, & \tau < \pi/2 \\ n, & (n-1/2)\pi < \tau < (n+1/2)\pi, \quad n = 1,2,3,\cdots \end{cases} \tag{4.10}$$

and

$$N_{TM} = \{n+1, \qquad n\pi < \tau < (n+1)\pi, \qquad n = 0,1,2,\cdots \tag{4.11}$$

where

$$\tau = k_o d\sqrt{\varepsilon_r - 1}$$

Since the first TM surface wave has a zero cutoff frequency, there is at least one singularity in the integration. Additional surface wave poles are introduced as the electrical thickness of the dielectric increases. In most applications, these higher-order surface waves are avoided.

Since there will always be at least one singularity present, it is necessary to develop a suitable technique to numerically evaluate the singular integrals. There are a couple of simple techniques that could be attempted. One is to add loss to the dielectric, thereby shifting the poles slightly off the path of integration. Another possibility is to deform the path of integration around the singularity by applying the Cauchy-Goursat theorem. However, it will be shown that the first method is inadequate, and the second method is not theoretically justified for the inner product definition (3.7).

The simplest technique to implement is adding loss to the dielectric substrate. The dielectric loss is easily included in the analysis by replacing ε_r in (2.6)-(2.9) by $\varepsilon_r(1-j\tan\delta)$, where $\tan\delta$ is the loss tangent of the dielectric substrate. This loss will move the poles off the real ρ axis so that the poles will occur at $\rho=\rho'-j\rho''$, $\rho''>0$. Since the path of integration is on the real ρ axis, the integral is theoretically nonsingular.

For realistic problems, however, the integrand is still poorly behaved for values of ρ near $\rho=\rho'$, because the poles do not move far off the real ρ axis unless the dielectric substrate is unrealistically lossy and/or thick. For example, consider a typical microstrip substrate of alumina ($\varepsilon_r=9.6$, $\tan\delta=10^{-4}$) that is 25 mils thick. An actual microstrip circuit designed on this substrate might operate at frequencies between 0 and 20 GHz. For this case, the location of the first TM surface wave pole is plotted in Fig. 4.1 for various substrate thicknesses and dielectric losses. The substrate thicknesses $d/\lambda_0=0.02$, 0.04, and 0.08 correspond to the operating frequencies of 9.5, 18.9, and 37.8 GHz, respectively. For each of these thicknesses, the real and imaginary parts of the pole are shown for the dielectric loss tangents of 10^{-6}, 10^{-4} and 10^{-2}. The figure shows that the imaginary part of the pole ρ'' increases when the electrical thickness or the loss tangent of the substrate is

increased. However, for a realistic case where $d/\lambda_o<0.1$ and $\tan\delta=10^{-4}$, ρ'' is small and the pole remains essentially real. In this case, the Green's function is still sharply peaked near the singularity. In Figs. 4.2-4.4, the component $\tilde{G}_{xx}$ of the Green's function is plotted for values of ρ near the singularity. Even for the thickest substrate in Fig. 4.4, the Green's function is not smooth enough to numerically integrate without an adaptive routine. Therefore, adding loss to the dielectric is not a viable technique.

Instead of integrating along the real ρ axis, an alternate integration path might be taken around the pole by applying the Cauchy-Goursat theorem [10]. This theorem states that if a function f(z) is analytic at all points interior to and on a simple closed contour C, then the contour integration of f(z) on C is zero. Expressed in another way, a line integral of f(z) is independent of path. In Fig. 4.5, the integration path b,c,d in the complex ρ plane is then equivalent to the original path a, provided the integrand is analytic and the dielectric is slightly lossy.

When this procedure was implemented in the evaluation of the inner products, it was found that the results obtained were incorrect. For instance, all of the inner products in which the testing function is identical to the basis function should be equal. However, all of these inner products, known as self-terms, were different when the integration path was deformed.

The problem with the contour deformation is better understood by first examining the moment method procedure in the spatial domain, and then determining how this relates to the spectral domain approach. In the spatial domain, the inner product is defined without the conjugation. As an example, the inner product for the x component is

$$\left\langle J_x^b, E_x^a \right\rangle = \int_{-\infty}^{\infty}\int_{-\infty}^{\infty} J_x^b(x,z)E_x^a(x,z)\,dxdz \qquad (4.12)$$

where E_x^a is the electric field due to the current source a. The inner product integral in (4.12) is equivalent to a reaction [11]. The reaction concept is useful, since it is consistent with the reciprocity theorem. For instance, the reaction of field a on source b is equal to the reaction of field b on source a. The resulting symmetries in the testing procedure can be used to reduce the number of inner products that need to be evaluated.

The physical insight gained from the spatial domain approach is directly applicable in the spectral domain, because these two approaches are actually equivalent. This equivalence is shown by applying Parseval's theorem to Equation (4.12) to give

$$\left\langle \tilde{J}_x^b, \tilde{E}_x^a \right\rangle = \frac{1}{4\pi^2} \int_{-\infty}^{\infty} \int_{-\infty}^{\infty} \tilde{J}_x^{b*}(\alpha,\beta) \tilde{E}_x^a(\alpha,\beta)\, d\alpha d\beta \tag{4.14}$$

where

$$\tilde{E}_x^a(\alpha,\beta) = \tilde{G}_{xx}(\alpha,\beta) \tilde{J}_x^a(\alpha,\beta) \tag{4.15}$$

Here, the spatial domain testing function J_x^b was assumed to be real, and the conjugation of $\tilde{J}_x^b$ is a result of Parseval's theorem. Except for the constant, the testing process in (4.14) is the same as for the inner product definition (3.7) adopted in this work. Therefore, the spectral and spatial domain approaches are analogous with this inner product definition.

Unfortunately, if the inner product definition is taken exactly as given in (3.7), it can be shown that the integrand is not analytic. The problem arises from the conjugation of the testing function in the inner product definition. When the integration variables are considered complex, the conjugated testing functions fail to satisfy the Cauchy-Riemann equations [12], a necessary condition for a function to be analytic. Since the integrand is not analytic, the contour deformation technique cannot be applied.

Although the contour deformation technique might be valid with a different inner product definition, we chose to integrate the singularity with an adaptive routine. In this way, the relationship between the spectral domain approach and the spatial domain

approach is definitely preserved. The numerical integrator used in the region near the singularity was an adaptive quadrature routine designed specifically for singularities.

4.3 Convergence Rate

When the basis functions described in Chapter 3 are used, the convergence rate of the inner product integrals is extremely slow. The primary reason for this is that the integrations over the ρ variable converge slowly near the α and β axes. Each of the basis functions $\tilde{J}_{xi}$ and $\tilde{J}_{zi}$ in Equations (3.16) and (3.17) contain a ρ^{-3} term in polar coordinates, but their actual rate of decay is much less than ρ^{-3} for some θ. For instance, the triangle function in $\tilde{J}_{xi}$ will tend to a constant near $\theta=0^{\circ}$ (the β axis) resulting in a rate of decay only slightly greater than ρ^{-1}. Another reason for the slow rate of convergence is that the basis functions are typically small in the spatial domain. The corresponding spectral domain basis functions are very broad and slowly decaying.

In an effort to increase the rate of convergence, higher-order basis functions were considered. The pulse function of (3.12) was replaced by a pulse convolved with a triangle, and the triangle function of (3.13) was replaced by a triangle convolved with a triangle. Each of the resulting basis functions contributed a ρ^{-7} term to the integrand, and the inner product computation time was reduced.

However, this method of increasing the rate of convergence suffers from the same problems associated with the original basis functions. The integrations over the ρ variable still converge more slowly near the α and β axes, and inner products with small basis functions tend to converge slowly. Since the rate of convergence with higher-order basis functions is still inadequate, a different method of accelerating the integrations is discussed in detail in Chapter 5. This method is based on extracting the asymptotic behavior of the integrand.

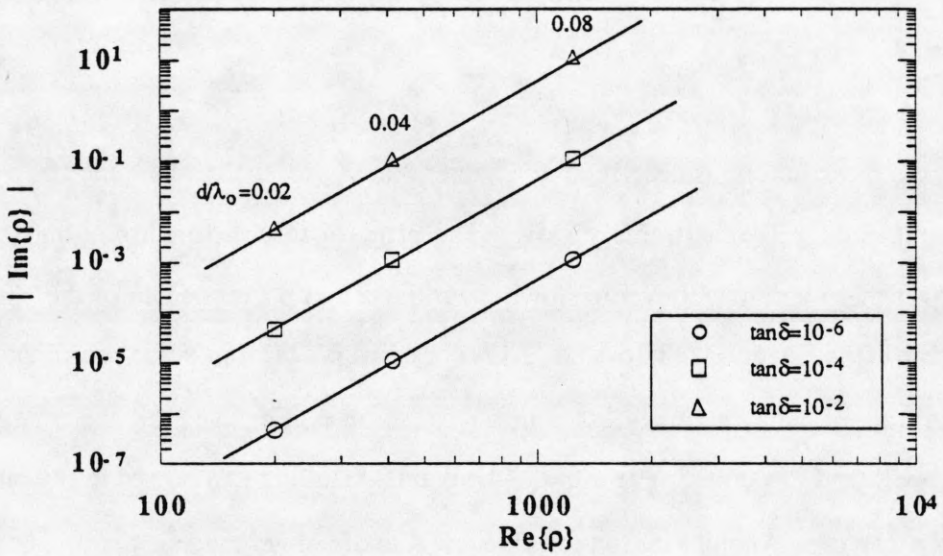

Figure 4.1. Location of the first TM surface wave pole for various substrate thicknesses and loss tangents (ε_r=9.6, d=25 mils).

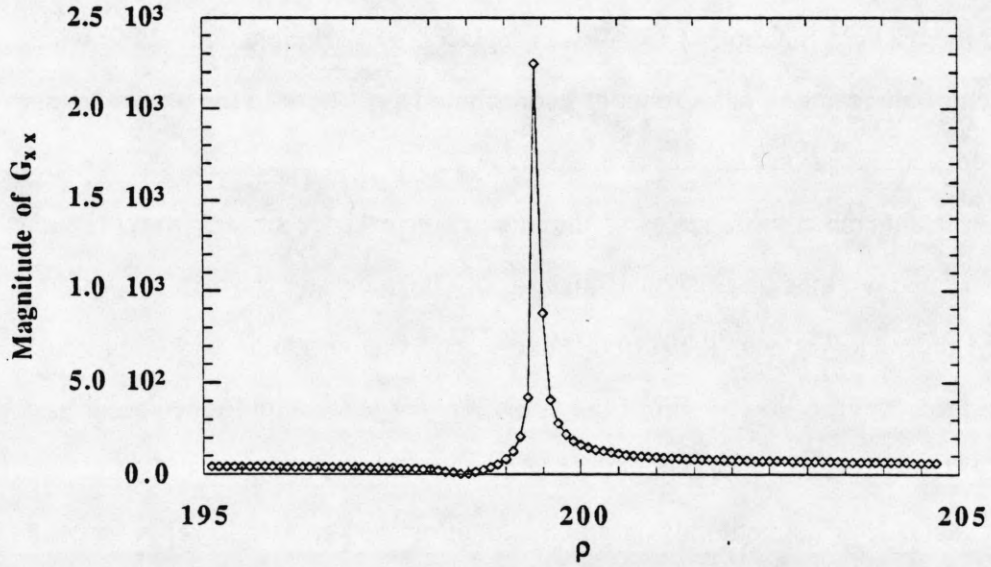

Figure 4.2. Magnitude of the Green's function near the TM surface wave pole for d/λ_0=0.02 (ε_r=9.6, d=25 mils, θ=45°).

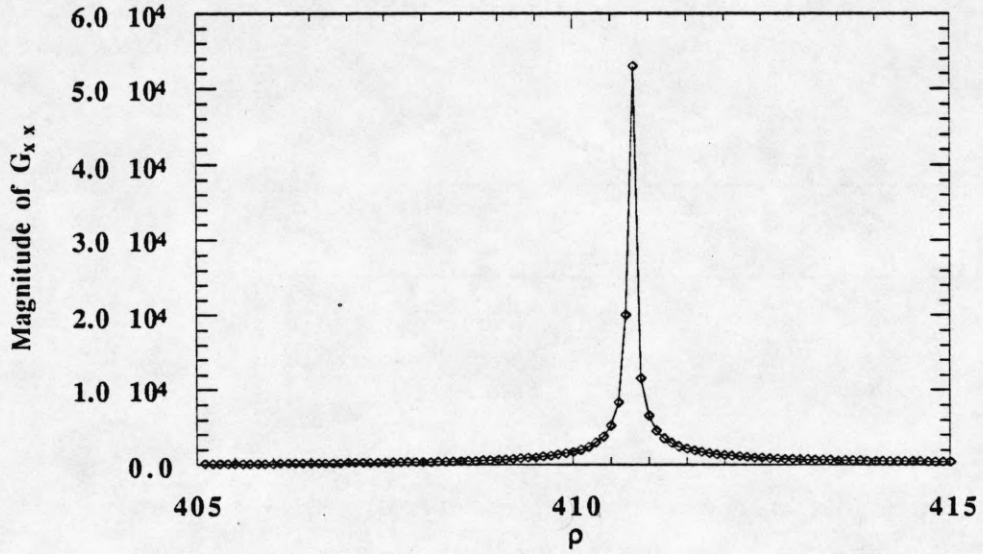

Figure 4.3. Magnitude of the Green's function near the TM surface wave pole for d/λ_o=0.04 (ε_r=9.6, d=25 mils, θ=45°).

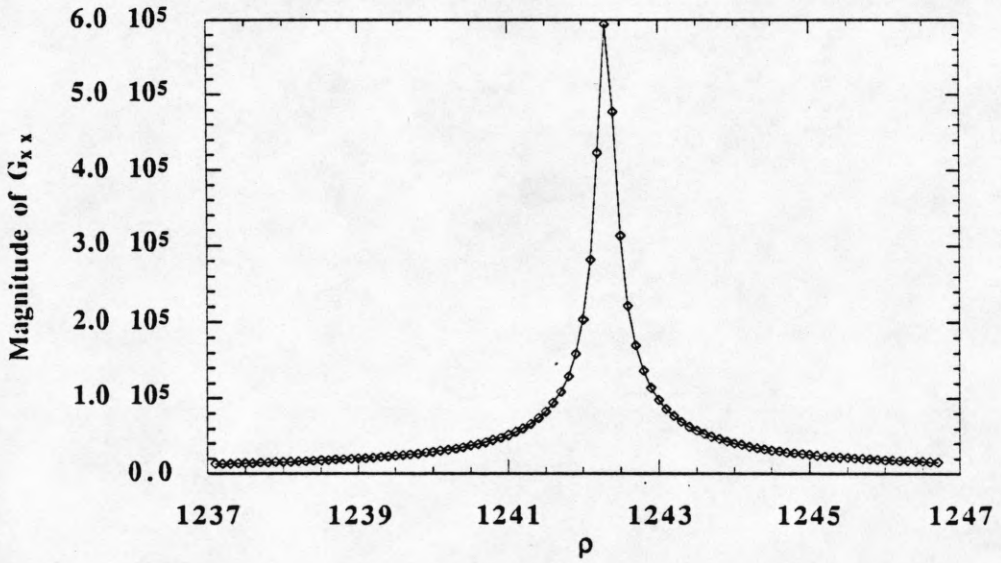

Figure 4.4. Magnitude of the Green's function near the TM surface wave pole for d/λ_o=0.08 (ε_r=9.6, d=25 mils, θ=45°).

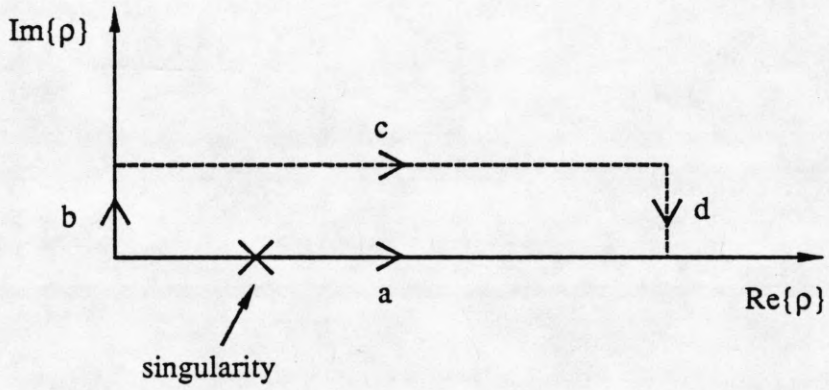

Figure 4.5. Original integration path a, through the singularity, and the alternate integration path b,c,d in the complex ρ plane.

CHAPTER 5

ASYMPTOTIC ACCELERATION TECHNIQUE

The most serious limitation of the spectral domain approach is the computation time required to evaluate the inner products. As discussed earlier, the inner products are doubly infinite integrals that are usually very slowly convergent. The convergence problem is not unique to the analysis of microstrip discontinuities, and work has been done to reduce the computation time in the analysis of periodic problems [2], such as arrays of scatterers and arrays of antennas. Although the inner products in these periodic problems are infinite sums rather than integrals, the general idea is the same. A suitable function is first subtracted from the integrand so that the integral will converge more rapidly. The function is then integrated separately and added back so that the original integral remains unchanged.

In this chapter, the acceleration technique is applied to the inner product integrals in order to increase their rate of convergence for the infinite rho integrations. In Section 5.1, the asymptotic form of the integrand is derived and then subtracted from the original integrand. As a consequence, the resulting integral will converge more rapidly. In order to recover the original inner product, the asymptotic form is integrated separately and added back. In Section 5.2, the integral of the asymptotic form is evaluated in closed form by deriving an equivalent integral in the spatial domain.

5.1 Asymptotic Form in the Spectral Domain

In applying the asymptotic acceleration technique, it is important to realize that any asymptotic expression can be subtracted from the integrand and added back on, without changing the original integral. However, a speedup in the overall computation is achieved only if the expression that is added back can be integrated efficiently. With this in mind, the asymptotic form of the integrand is derived by determining the asymptotic behavior of the Green's function and then multiplying this by the basis and testing functions. In this

way, the asymptotic form is simplified, and the integral of the asymptotic form may be evaluated in closed form.

The derivation of the asymptotic form of the Green's function is relatively straightforward. The behavior of each term of the Green's function in (2.6)-(2.9) is determined first, and then the overall asymptotic behavior of the Green's function is deduced. For large ρ, the terms s and s′ are, to first order,

$$s = -j\sqrt{\rho^2 - k_o^2} \approx -j\rho \tag{5.1}$$

$$s' = -j\sqrt{\rho^2 - k_o^2} \approx -j\rho \tag{5.2}$$

Inserting (5.1) and (5.2) into the terms D_1, D_2 and D_3 yields

$$D_1 \approx -j\rho(1+\varepsilon_r) \tag{5.3}$$

$$D_2 \approx -2j\rho \tag{5.4}$$

$$D_3 \approx -2j\rho \tag{5.5}$$

With the substitution, the term cot(s′d) in D_1, D_2, and D_3 becomes jcoth(ρd). The hyperbolic cotangent is then approximated as 1 for large ρ. Finally, Equations (5.3)-(5.4) are substituted into the expressions for the Green's function in (2.6)-(2.9), resulting in the asymptotic Green's function denoted as

$$\tilde{G}^a_{xx}(\rho,\theta) \equiv \frac{j}{\omega\varepsilon_o\rho}\left(\frac{\rho^2\sin^2(\theta)}{1+\varepsilon_r} - \frac{k_o^2}{2}\right) \tag{5.6}$$

$$\tilde{G}^a_{xz}(\rho,\theta) \equiv \frac{j}{\omega\varepsilon_o\rho}\left(\frac{\rho^2\sin(\theta)\cos(\theta)}{1+\varepsilon_r}\right) \tag{5.7}$$

$$\tilde{G}^a_{zx}(\rho,\theta) \equiv \tilde{G}^a_{xz}(\rho,\theta) \tag{5.8}$$

$$\tilde{G}^a_{zz}(\rho,\theta) \equiv \frac{j}{\omega\varepsilon_o\rho}\left(\frac{\rho^2\cos^2(\theta)}{1+\varepsilon_r} - \frac{k_o^2}{2}\right) \tag{5.9}$$

The asymptotic form of the integrand is derived by multiplying the asymptotic Green's function in (5.6)-(5.9) by the appropriate basis and testing functions in the inner product. This asymptotic form is then subtracted from the original inner product integrals and added back to give

$$\left\langle \tilde{J}_{xj}, \tilde{G}_{xx}\tilde{J}_{xi} \right\rangle = \int_0^{2\pi}\int_0^{\infty} \tilde{J}^*_{xj}\left(\tilde{G}_{xx} - \tilde{G}^a_{xx}\right)\tilde{J}_{xi}\,\rho d\rho d\theta + \int_0^{2\pi}\int_0^{\infty} \tilde{J}^*_{xj}\tilde{G}^a_{xx}\tilde{J}_{xi}\,\rho d\rho d\theta \tag{5.10}$$

$$\left\langle \tilde{J}_{xj}, \tilde{G}_{xz}\tilde{J}_{zi} \right\rangle = \int_0^{2\pi}\int_0^{\infty} \tilde{J}^*_{xj}\left(\tilde{G}_{xz} - \tilde{G}^a_{xz}\right)\tilde{J}_{zi}\,\rho d\rho d\theta + \int_0^{2\pi}\int_0^{\infty} \tilde{J}^*_{xj}\tilde{G}^a_{xz}\tilde{J}_{zi}\,\rho d\rho d\theta \tag{5.11}$$

$$\left\langle \tilde{J}_{zj}, \tilde{G}_{zz}\tilde{J}_{zi} \right\rangle = \int_0^{2\pi}\int_0^{\infty} \tilde{J}^*_{zj}\left(\tilde{G}_{zz} - \tilde{G}^a_{zz}\right)\tilde{J}_{zi}\,\rho d\rho d\theta + \int_0^{2\pi}\int_0^{\infty} \tilde{J}^*_{zj}\tilde{G}^a_{zz}\tilde{J}_{zi}\,\rho d\rho d\theta \tag{5.12}$$

where the arguments of the functions have been dropped for brevity. The inner product $\langle \tilde{J}_{zj}, \tilde{G}_{zx}\tilde{J}_{xi} \rangle$ will no longer be discussed, since it is identical in form to (5.11). Although the limits of integration shown in (5.10)-(5.12) encompass the entire plane, these limits can be reduced to only the first quadrant. The results of Section 4.1 can be applied directly to the integrals, since the symmetries in the integrands are unchanged.

By subtracting the asymptotic form, the rate of convergence for the first integral in (5.10)-(5.12) is accelerated. As the Green's function approaches its asymptotic limit for large ρ, the entire integrand will go to zero. The second integral in each inner product is the asymptotic form that has been added back. In order to substantially reduce the overall computation time, the second integral must be computed efficiently. In the following section, these integrals are evaluated in closed form in the spatial domain.

It is important to note that the asymptotic form derived in this section is a first-order expression. For instance, the radicals in (5.1) and (5.2) and the term $\coth(\rho d)$ were

approximated by only the first term in the series expansions for these functions. Although an asymptotic form containing higher-order terms will increase the rate of convergence of the first integral in (5.10)-(5.12), a price is paid since the second integral will be considerably more complicated. If the second integral must be evaluated numerically, little or no speedup in the overall computation may be realized.

Even with a first-order approximation, the Green's function approaches its asymptotic form fairly rapidly. As an example, the component $\tilde{G}_{xx}$ of the Green's function is plotted along with $\tilde{G}_{xx}$-$\tilde{G}^a_{xx}$ for different theta cuts in Figs. 5.1-5.3. It is apparent from these plots that the asymptotic acceleration technique will increase the rate of convergence for the rho integrations for all values of theta. This is a substantial improvement over the technique discussed in Section 4.3 in which higher-order basis functions are used to accelerate the rate of convergence. With that technique, the rate of convergence was not improved significantly for values of theta near 0° or 90°. Another advantage of the asymptotic acceleration technique is that the acceleration is dependent on the Green's function and not on the basis functions. Therefore, the inner product integrations with small spatial domain basis functions will also converge rapidly, even though the corresponding spectral domain basis functions are very broad.

5.2 Analytic Integration of the Asymptotic Form

The most difficult step in applying the asymptotic acceleration technique is evaluating the integral of the asymptotic form. This integral is the second integral in Equations (5.10)-(5.12). The procedure used to evaluate the integrals is summarized as follows. The terms in the integrand are first grouped into two functions, and then Parseval's theorem is applied to derive an equivalent integral in the spatial domain. The advantage of evaluating the integral in the spatial domain is that the limits of integration are then finite. At this point, the integrals might be computed numerically. However, these spatial domain integrals are evaluated analytically in closed form. In this way, the

computation time is reduced to a minimum and no additional error is introduced in adding back the asymptotic form.

In order to develop the notation for the following discussion, Parseval's theorem is first stated: If $\tilde{U}(\alpha,\beta)$ and $\tilde{V}(\alpha,\beta)$ are Fourier transforms of u(x,z) and v(x,z), respectively, then

$$\int_{-\infty}^{\infty}\int_{-\infty}^{\infty} u^*(x,z)\,v(x,z)\,dxdz = \frac{1}{4\pi^2}\int_{-\infty}^{\infty}\int_{-\infty}^{\infty} \tilde{U}^*(\alpha,\beta)\,\tilde{V}(\alpha,\beta)\,d\alpha d\beta \tag{5.13}$$

In the analysis, the integrals in (5.10)-(5.12) will be considered in Cartesian coordinates so that Parseval's theorem and other Fourier transform properties may be applied.

The terms in each integrand are now grouped to form two functions corresponding to the functions $\tilde{U}^*(\alpha,\beta)$ and $\tilde{V}(\alpha,\beta)$ in (5.13). When grouping the terms, particular attention must be paid to insure that each of the resulting functions has an inverse transform that exists. With this in mind, the asymptotic integrals in (5.10)-(5.12) are rewritten as

$$\begin{aligned}\left\langle \tilde{J}_{xj}, \tilde{G}^a_{xx}\tilde{J}_{xi}\right\rangle = {} & \frac{j}{\omega\varepsilon_o(1+\varepsilon_r)}\int_{-\infty}^{\infty}\int_{-\infty}^{\infty}\left(\frac{1}{\sqrt{\alpha^2+\beta^2}}\right)\left(\alpha^2\,\tilde{\Lambda}^2_{w_x}(\alpha)\,\tilde{\Pi}^2_{t_x}(\beta)\,e^{-j(\alpha x'+\beta z')}\right)d\alpha d\beta \\ & -\frac{jk_o^2}{2\omega\varepsilon_o}\int_{-\infty}^{\infty}\int_{-\infty}^{\infty}\left(\frac{1}{\sqrt{\alpha^2+\beta^2}}\right)\left(\tilde{\Lambda}^2_{w_x}(\alpha)\,\tilde{\Pi}^2_{t_x}(\beta)\,e^{-j(\alpha x'+\beta z')}\right)d\alpha d\beta\end{aligned} \tag{5.14}$$

$$\begin{aligned}\left\langle \tilde{J}_{xj}, \tilde{G}^a_{xz}\tilde{J}_{zi}\right\rangle = {} & \frac{j}{\omega\varepsilon_o(1+\varepsilon_r)}\int_{-\infty}^{\infty}\int_{-\infty}^{\infty}\left(\frac{1}{\sqrt{\alpha^2+\beta^2}}\right)\Big(\alpha\beta\,\tilde{\Lambda}_{w_x}(\alpha)\,\tilde{\Pi}_{t_z}(\alpha) \\ & \times \tilde{\Lambda}_{w_z}(\beta)\,\tilde{\Pi}_{t_x}(\beta)\,e^{-j(\alpha x'+\beta z')}\Big)d\alpha d\beta\end{aligned} \tag{5.15}$$

$$\left\langle \tilde{J}_{zj}, \tilde{G}^{a}_{zz} \tilde{J}_{zi} \right\rangle = \frac{j}{\omega\varepsilon_o(1+\varepsilon_r)} \int_{-\infty}^{\infty}\int_{-\infty}^{\infty} \left(\frac{1}{\sqrt{\alpha^2+\beta^2}} \right) \left(\beta^2 \tilde{\Lambda}^2_{w_z}(\beta) \tilde{\Pi}^2_{t_z}(\alpha) e^{-j(\alpha x'+\beta z')} \right) d\alpha d\beta$$
$$- \frac{jk_o^2}{2\omega\varepsilon_o} \int_{-\infty}^{\infty}\int_{-\infty}^{\infty} \left(\frac{1}{\sqrt{\alpha^2+\beta^2}} \right) \left(\tilde{\Lambda}^2_{w_z}(\beta) \tilde{\Pi}^2_{t_z}(\alpha) e^{-j(\alpha x'+\beta z')} \right) d\alpha d\beta \qquad (5.16)$$

where

$$x' = (x_i - x_j)$$
$$z' = (z_i - z_j)$$

and where the functions corresponding to $\tilde{U}^*(\alpha,\beta)$ and $\tilde{V}(\alpha,\beta)$ in (5.13) are separated by parentheses. The terms α^2,β^2, and $\alpha\beta$ from the asymptotic Green's function have been grouped with the basis and testing functions to form the function $\tilde{V}(\alpha,\beta)$. The terms were grouped in this manner, because the inverse transform of the entire asymptotic Green's function does not exist. The remaining function $1/\sqrt{\alpha^2+\beta^2}$ corresponds to the function $\tilde{U}^*(\alpha,\beta)$. Since this function is real, the conjugation is dropped to simplify the notation.

The functions u(x,z) and v(x,z), the inverse transforms of the functions $\tilde{U}(\alpha,\beta)$ and $\tilde{V}(\alpha,\beta)$, are needed to continue the derivation of the equivalent spatial domain integral. The inverse transform of $\tilde{U}$ is considered first and is given by

$$u(x,z) = \frac{1}{4\pi^2} \int_{-\infty}^{\infty}\int_{-\infty}^{\infty} \frac{1}{\sqrt{\alpha^2+\beta^2}} e^{j(\alpha x+\beta z)} d\alpha d\beta \qquad (5.17)$$

The integral in (5.17) is then converted into polar coordinates in both the spectral and spatial domain variables [13]. Making the substitutions $\alpha=\rho\sin\theta$, $\beta=\rho\cos\theta$, $x=r\sin\phi$, and $z=r\cos\phi$ leads to

$$u(r,\phi) = \frac{1}{4\pi^2} \int_{0}^{2\pi}\int_{0}^{\infty} e^{j\rho r\cos(\theta-\phi)} d\rho d\theta \qquad (5.18)$$

where a trigonometric identity was used to simplify the argument of the exponent. The integral over the variable θ in (5.18) is recognized as the Bessel function $J_0(\rho r)$. Making this substitution and using the fact that $\int_0^\infty J_0(t)dt=1$ yield the inverse transform

$$u(x,z) = \frac{1}{2\pi\sqrt{x^2+z^2}} \tag{5.19}$$

Determining the inverse transforms of the functions corresponding to $\tilde{V}(\alpha,\beta)$ is considerably more tedious. In the spectral domain, these functions are denoted as

$$\tilde{V}_1(\alpha,\beta) = \alpha^2 \tilde{\Lambda}^2_{w_x}(\alpha)\tilde{\Pi}^2_{t_x}(\beta)e^{-j(\alpha x'+\beta z')} \tag{5.20}$$

$$\tilde{V}_2(\alpha,\beta) = \tilde{\Lambda}^2_{w_x}(\alpha)\tilde{\Pi}^2_{t_x}(\beta)e^{-j(\alpha x'+\beta z')} \tag{5.21}$$

$$\tilde{V}_3(\alpha,\beta) = \alpha\beta\tilde{\Lambda}_{w_x}(\alpha)\tilde{\Pi}_{t_z}(\alpha)\tilde{\Lambda}_{w_z}(\beta)\tilde{\Pi}_{t_x}(\beta)e^{-j(\alpha x'+\beta z')} \tag{5.22}$$

$$\tilde{V}_4(\alpha,\beta) = \beta^2 \tilde{\Lambda}^2_{w_z}(\beta)\tilde{\Pi}^2_{t_z}(\alpha)e^{-j(\alpha x'+\beta z')} \tag{5.23}$$

$$\tilde{V}_5(\alpha,\beta) = \tilde{\Lambda}^2_{w_z}(\beta)\tilde{\Pi}^2_{t_z}(\alpha)e^{-j(\alpha x'+\beta z')} \tag{5.24}$$

After applying several Fourier transform properties, the inverse transforms of the functions in Equations (5 20)-(5.24) can be represented as

$$v_1(x,z) = -\frac{\partial^2}{\partial x^2}\left[\Lambda_{w_x}(x-x')*\Lambda_{w_x}(x-x')\,\Pi_{t_x}(z-z')*\Pi_{t_x}(z-z')\right] \tag{5.25}$$

$$v_2(x,z) = \left[\Lambda_{w_x}(x-x')*\Lambda_{w_x}(x-x')\,\Pi_{t_x}(z-z')*\Pi_{t_x}(z-z')\right] \tag{5.26}$$

$$v_3(x,z) = -\frac{\partial^2}{\partial x\partial z}\left[\Lambda_{w_x}(x-x')*\Pi_{t_z}(x-x')\,\Lambda_{w_z}(z-z')*\Pi_{t_x}(z-z')\right] \tag{5.27}$$

$$v_4(x,z) = -\frac{\partial^2}{\partial z^2}\left[\Pi_{t_z}(x-x')*\Pi_{t_z}(x-x')\,\Lambda_{w_z}(z-z')*\Lambda_{w_z}(z-z')\right] \tag{5.28}$$

$$v_5(x,z) = \left[\Pi_{t_z}(x-x')*\Pi_{t_z}(x-x')\,\Lambda_{w_z}(z-z')*\Lambda_{w_z}(z-z')\right] \tag{5.29}$$

In (5.25)-(5.26), the partial derivatives in the spatial domain correspond to the multiplication by α or β in the spectral domain. The convolutions of pulse and triangle functions result from the multiplication of their transforms in the spectral domain. Each of these convolutions is performed over only one spatial variable, because the functions are separable. Finally, the arguments of these functions are shifted in the spatial domain due to the exponential term in the spectral domain.

At this point, deriving the final expressions for the inverse transforms is primarily an exercise in algebra. The various convolutions between the triangle and pulse functions that are required are given in Table 5.1. Inserting these convolutions into equations (5.25)-(5.29) and performing the indicated differentiations will lead to the final expressions for the inverse transforms of $v_i(x,z)$. Since these expressions are fairly lengthy, they are not presented here explicitly.

Once the functions corresponding to $u(x,z)$ and $v(x,z)$ are determined, the equivalent asymptotic integrals in the spatial domain are known from (5.13). These spatial domain integrals have finite limits of the integration that are determined by the convolutions of the pulse and triangle functions. Since these convolutions result in piecewise continuous functions, the integrals are actually broken up into a sum of integrals with limits over smaller rectangular regions.

The types of integrals that need to be evaluated are polynomials in x and z divided by the function $1/\sqrt{x^2+z^2}$. The polynomials are a result of the convolutions in the functions v_i, and the radical comes from the function u in Equation (5.19). Most of these integrals can be found in standard integral tables, but several of these integrals required considerable effort to evaluate. All of the general integral types needed are listed in Table 5.2 in the form of definite integrals. In this table, $I_i(x_1,x_2,z_1,z_2)$ denotes the ith integral type, where (x_1,x_2) and (z_1,z_2) are the limits of the x and z integrations.

When Equations (5.19) and (5.25)-(5.29) are combined together with (5.13) and the integrals in Tables 5.1 and 5.2, a closed-form expression for the integral of the

asymptotic form is obtained. The asymptotic integral for the inner product $\langle \tilde{J}_{xj}, \tilde{G}_{xx} \tilde{J}_{xi} \rangle$ is expressed in compact form as

$$\left\langle \tilde{J}_{xj}, \tilde{G}^{a}_{xx} \tilde{J}_{xi} \right\rangle = 4\pi^2 \left\{ \frac{j}{\omega \varepsilon_o (1+\varepsilon_r)} I - \frac{j k_o^2}{2\omega\varepsilon_o} \hat{I} \right\} \tag{5.30}$$

where the integrals I and $\hat{I}$ are given in Table 5.3. The expression for the asymptotic integral $\langle \tilde{J}_{zj}, \tilde{G}^{a}_{zz} \tilde{J}_{zi} \rangle$ is obtained from (5.30) by replacing x by z and z by x. Finally, the asymptotic integral for the inner product $\langle \tilde{J}_{xj}, \tilde{G}_{xz} \tilde{J}_{zi} \rangle$ is

$$\left\langle \tilde{J}_{xj}, \tilde{G}^{a}_{xz} \tilde{J}_{zi} \right\rangle = 4\pi^2 \left\{ \frac{j}{\omega \varepsilon_o (1+\varepsilon_r)} \bar{I} \right\} \tag{5.31}$$

where the integral $\bar{I}$ is given in Table 5.4. For this integral, there are six different cases depending on the relative widths and thicknesses of the basis and testing functions.

Since the derivation of these expressions was rather involved, the final expressions for the asymptotic integrals were verified by direct numerical evaluation of the spectral domain integrals in Equations (5.14) and (5.15). As a test case, the substrate was chosen to be 1.57 mm thick with a relative dielectric constant of 4. The operating frequency is 1GHz, and the relative position (x′,z′) of the basis and testing functions is (0.3,0.4). For this test case, the results obtained from the analytic expressions and the numerical integrations are shown in Table 5.5. All of the analytic and numerical results are seen to agree within 2 percent. The difference is easily accounted for by the error in the numerical integration, because the integrand of the asymptotic form is poorly behaved. Therefore, the analytic expressions for the asymptotic integrals appear to be correct.

In Chapter 6, the performance of the asymptotic acceleration technique is evaluated by comparing the results of a routine that uses the technique and one that does not.

Table 5.1. Various convolutions of the pulse function and the triangle function.

Convolution of a Pulse with a Pulse:

$$\Pi_T(t)*\Pi_T(t)=\begin{cases}T+t, & -T\le t<0\\ T-t, & 0\le t\le T\end{cases}$$

Convolution of a Triangle with a Triangle:

$$\Lambda_w(t)*\Lambda_w(t)=\begin{cases}\dfrac{(2w+t)^3}{6w^2}, & -2w\le t<-w\\ -\dfrac{t^3}{2w^2}-\dfrac{t^2}{w}+\dfrac{2w}{3}, & -w\le t<0\\ \dfrac{t^3}{2w^2}-\dfrac{t^2}{w}+\dfrac{2w}{3}, & 0\le t<w\\ \dfrac{(2w-t)^3}{6w^2}, & w\le t\le 2w\end{cases}$$

Convolution of a Triangle with a Pulse:

Case 1: T<w

$$\Lambda_w(t)*\Pi_T(t)=\begin{cases}\dfrac{(T+2w+2t)^2}{8w}, & -(w+T/2)\le t<-(w-T/2)\\ T+\dfrac{T}{w}t, & -(w-T/2)\le t<-T/2\\ T-\dfrac{T^2}{4w}-\dfrac{t^2}{w}, & -T/2\le t<T/2\\ T-\dfrac{T}{w}t, & T/2\le t<(w-T/2)\\ \dfrac{(T+2w-2t)^2}{8w}, & (w-T/2)\le t\le(w+T/2)\end{cases}$$

Table 5.1 (Cont.)

Case 2: $w \le T \le 2w$

$$\Lambda_w(t) * \Pi_T(t) = \begin{cases} \dfrac{(T+2w+2t)^2}{8w}, & -(w+T/2) \le t < -T/2 \\ \dfrac{T+w}{2} + t - \dfrac{(T/2+t)^2}{2w}, & -T/2 \le t < -(w-T/2) \\ T - \dfrac{T^2}{4w} - \dfrac{t^2}{w}, & -(w-T/2) \le t < (w-T/2) \\ \dfrac{T+w}{2} - t - \dfrac{(T/2-t)^2}{2w}, & (w-T/2) \le t < T/2 \\ \dfrac{(T+2w-2t)^2}{8w}, & T/2 \le t \le (w+T/2) \end{cases}$$

Case 3: $T > 2w$

$$\Lambda_w(t) * \Pi_T(t) = \begin{cases} \dfrac{(T+2w+2t)^2}{8w}, & -(w+T/2) \le t < -T/2 \\ \dfrac{T+w}{2} + t - \dfrac{(T/2+t)^2}{2w}, & -T/2 \le t < -(T/2-w) \\ w, & -(T/2-w) \le t < (T/2-w) \\ \dfrac{T+w}{2} - t - \dfrac{(T/2-t)^2}{2w}, & (T/2-w) \le t < T/2 \\ \dfrac{(T+2w-2t)^2}{8w}, & T/2 \le t \le (w+T/2) \end{cases}$$

Table 5.2 Definite integrals needed in the integration of the asymptotic form.

$$I_1(x_1,x_2,z_1,z_2) = \int_{z_1}^{z_2}\int_{x_1}^{x_2} \frac{1}{\sqrt{x^2+z^2}}\,dxdz$$

$$= z\left[\ln\left(x+\sqrt{x^2+z^2}\right)-1\right]+x\ln\left(z+\sqrt{x^2+z^2}\right)\Bigg|_{x_1}^{x_2}\Bigg|_{z_1}^{z_2}$$

$$I_2(x_1,x_2,z_1,z_2) = \int_{z_1}^{z_2}\int_{x_1}^{x_2} \frac{x}{\sqrt{x^2+z^2}}\,dxdz$$

$$= \frac{1}{2}\left[z\sqrt{x^2+z^2}+x^2\ln\left(z+\sqrt{x^2+z^2}\right)\right]\Bigg|_{x_1}^{x_2}\Bigg|_{z_1}^{z_2}$$

$$I_3(x_1,x_2,z_1,z_2) = \int_{z_1}^{z_2}\int_{x_1}^{x_2} \frac{x^2}{\sqrt{x^2+z^2}}\,dxdz$$

$$= \frac{zx}{6}\sqrt{x^2+z^2}-\frac{x^3}{9}+\frac{x^3}{3}\ln\left(z+\sqrt{x^2+z^2}\right)-\frac{z^3}{6}\ln\left(x+\sqrt{x^2+z^2}\right)\Bigg|_{x_1}^{x_2}\Bigg|_{z_1}^{z_2}$$

$$I_4(x_1,x_2,z_1,z_2) = \int_{z_1}^{z_2}\int_{x_1}^{x_2} \frac{x^3}{\sqrt{x^2+z^2}}\,dxdz$$

$$= -\frac{z}{6}\left(x^2+z^2\right)^{\frac{3}{2}}+\frac{x^2z}{4}\sqrt{x^2+z^2}+\frac{x^4}{4}\ln\left(z+\sqrt{x^2+z^2}\right)\Bigg|_{x_1}^{x_2}\Bigg|_{z_1}^{z_2}$$

$$I_5(x_1,x_2,z_1,z_2) = \int_{z_1}^{z_2}\int_{x_1}^{x_2} \frac{xz}{\sqrt{x^2+z^2}}\,dxdz$$

$$= \frac{1}{3}\left(x^2+z^2\right)^{\frac{3}{2}}\Bigg|_{x_1}^{x_2}\Bigg|_{z_1}^{z_2}$$

Table 5.2 (Cont.)

$$I_6(x_1,x_2,z_1,z_2) = \int_{z_1}^{z_2}\int_{x_1}^{x_2} \frac{x^2 z}{\sqrt{x^2+z^2}}\,dxdz$$

$$= \frac{x}{4}\left(x^2+z^2\right)^{\frac{3}{2}} - \frac{z^2 x}{8}\sqrt{x^2+z^2} - \frac{z^4}{8}\ln\left(x+\sqrt{x^2+z^2}\right)\Bigg|_{x_1}^{x_2}\Bigg|_{z_1}^{z_2}$$

$$I_7(x_1,x_2,z_1,z_2) = \int_{z_1}^{z_2}\int_{x_1}^{x_2} \frac{x^3 z}{\sqrt{x^2+z^2}}\,dxdz$$

$$= \frac{1}{15}\left(3x^2-2z^2\right)\left(x^2+z^2\right)^{\frac{3}{2}}\Bigg|_{x_1}^{x_2}\Bigg|_{z_1}^{z_2}$$

Table 5.3 Expressions for the integrals I and $\hat{I}$ in Equation (5.30). The definite integrals I_i appearing in this table are defined in Table 5.2.

$$I = \frac{-1}{2\pi}(a+b)$$

$$\hat{I} = \frac{1}{2\pi}\left(\hat{a}+\hat{b}+\hat{c}+\hat{d}\right)$$

where

$$a = \sum_{i=1}^{4} a_i\left[I_5(x_i,x_{i+1},z_1,z_2) - I_5(x_i,x_{i+1},z_2,z_3) + \tau I_2(x_i,x_{i+1},z_1,z_2) + \kappa I_2(x_i,x_{i+1},z_2,z_3)\right]$$

$$b = \sum_{i=1}^{4} b_i\left[I_2(z_1,z_2,x_i,x_{i+1}) - I_2(z_2,z_3,x_i,x_{i+1}) + \tau I_1(z_1,z_2,x_i,x_{i+1}) + \kappa I_1(z_2,z_3,x_i,x_{i+1})\right]$$

$$\hat{a} = \sum_{i=1}^{4} \hat{a}_i\left[I_7(x_i,x_{i+1},z_1,z_2) - I_7(x_i,x_{i+1},z_2,z_3) + \tau I_4(x_i,x_{i+1},z_1,z_2) + \kappa I_4(x_i,x_{i+1},z_2,z_3)\right]$$

$$\hat{b} = \sum_{i=1}^{4} \hat{b}_i\left[I_6(x_i,x_{i+1},z_1,z_2) - I_6(x_i,x_{i+1},z_2,z_3) + \tau I_3(x_i,x_{i+1},z_1,z_2) + \kappa I_3(x_i,x_{i+1},z_2,z_3)\right]$$

$$\hat{c} = \sum_{i=1}^{4} \hat{c}_i\left[I_5(x_i,x_{i+1},z_1,z_2) - I_5(x_i,x_{i+1},z_2,z_3) + \tau I_2(x_i,x_{i+1},z_1,z_2) + \kappa I_2(x_i,x_{i+1},z_2,z_3)\right]$$

$$\hat{d} = \sum_{i=1}^{4} \hat{d}_i\left[I_2(z_1,z_2,x_i,x_{i+1}) - I_2(z_2,z_3,x_i,x_{i+1}) + \tau I_1(z_1,z_2,x_i,x_{i+1}) + \kappa I_1(z_2,z_3,x_i,x_{i+1})\right]$$

and where

$$\tau = t_x - z' \qquad \kappa = t_x + z'$$

$$x_1 = x' - 2w_x \qquad z_1 = z' - t_x$$
$$x_2 = x' - w_x \qquad z_2 = z'$$
$$x_3 = x' \qquad z_3 = z' + t_x$$
$$x_4 = x' + w_x$$
$$x_5 = x' + 2w_x$$

Table 5.3 (Cont.)

$$a_1 = \frac{1}{w_x^2} \qquad b_1 = \frac{2}{w_x} - \frac{x'}{w_x^2}$$

$$a_2 = \frac{-3}{w_x^2} \qquad b_2 = \frac{-2}{w_x} + \frac{3x'}{w_x^2}$$

$$a_3 = -a_2 \qquad b_3 = \frac{-2}{w_x} - \frac{3x'}{w_x^2}$$

$$a_4 = -a_1 \qquad b_4 = \frac{2}{w_x} + \frac{x'}{w_x^2}$$

$$\hat{a}_1 = \frac{1}{6w_x^2} \qquad \hat{b}_1 = \frac{1}{w_x} - \frac{x'}{2w_x^2}$$

$$\hat{a}_2 = \frac{-1}{2w_x^2} \qquad \hat{b}_2 = \frac{-1}{w_x} + \frac{3x'}{2w_x^2}$$

$$\hat{a}_3 = -a_2 \qquad \hat{b}_3 = \frac{-1}{w_x} - \frac{3x'}{2w_x^2}$$

$$\hat{a}_4 = -a_1 \qquad \hat{b}_4 = \frac{1}{w_x} + \frac{x'}{2w_x^2}$$

$$\hat{c}_1 = 2 - \frac{2x'}{w_x} + \frac{x'^2}{2w_x^2} \qquad \hat{d}_1 = -2x' + \frac{4w_x}{3} + \frac{x'^2}{w_x} - \frac{x'^3}{6w_x^2}$$

$$\hat{c}_2 = \frac{2x'}{w_x} - \frac{3x'^2}{2w_x^2} \qquad \hat{d}_2 = \frac{2w_x}{3} - \frac{x'^2}{w_x} + \frac{x'^3}{2w_x^2}$$

$$\hat{c}_3 = \frac{2x'}{w_x} + \frac{3x'^2}{2w_x^2} \qquad \hat{d}_3 = \frac{2w_x}{3} - \frac{x'^2}{w_x} - \frac{x'^3}{2w_x^2}$$

$$\hat{c}_4 = -2 - \frac{2x'}{w_x} - \frac{x'^2}{2w_x^2} \qquad \hat{d}_4 = 2x' + \frac{4w_x}{3} + \frac{x'^2}{w_x} + \frac{x'^3}{6w_x^2}$$

Table 5.4 Expression for the integral $\bar{I}$ in Equation (5.31). The definite integrals I_i appearing in this table are defined in Table 5.2.

$$\bar{I} = \frac{-1}{2\pi}\sum_{j=1}^{5}\sum_{i=1}^{5}\Big\{a_{iz}\Big[a_{jx}\,I_5(x_j,x_{j+1},z_i,z_{i+1}) + b_{jx}\,I_2(z_i,z_{i+1},x_j,x_{j+1})\Big] + b_{iz}\Big[a_{jx}\,I_2(x_j,x_{j+1},z_i,z_{i+1}) + b_{jx}\,I_1(x_j,x_{j+1},z_i,z_{i+1})\Big]\Big\}$$

where the variables $x_j, z_i, a_{jx}, b_{jx}, a_{iz}$, and b_{iz} are listed below for each of the six different cases.

Case 1: $t_z \le w_x$ and $t_x \le w_z$

$$x_1 = x' - (w_x + t_z/2) \qquad z_1 = z' - (w_z + t_x/2)$$
$$x_2 = x' - (w_x - t_z/2) \qquad z_2 = z' - (w_z - t_x/2)$$
$$x_3 = x' - t_z/2 \qquad z_3 = z' - t_x/2$$
$$x_4 = x' + t_z/2 \qquad z_4 = z' + t_x/2$$
$$x_5 = x' + (w_x - t_z/2) \qquad z_5 = z' + (w_z - t_x/2)$$
$$x_6 = x' + (w_x + t_z/2) \qquad z_6 = z' + (w_z + t_x/2)$$

$$a_{1x} = \frac{1}{w_x} \qquad b_{1x} = \frac{t_z}{2w_x} - \frac{x'}{w_x} + 1 \qquad a_{1z} = \frac{1}{w_z} \qquad b_{1z} = \frac{t_x}{2w_z} - \frac{z'}{w_z} + 1$$

$$a_{2x} = 0 \qquad b_{2x} = \frac{t_z}{w_x} \qquad a_{2z} = 0 \qquad b_{2z} = \frac{t_x}{w_z}$$

$$a_{3x} = \frac{-2}{w_x} \qquad b_{3x} = \frac{2x'}{w_x} \qquad a_{3z} = \frac{-2}{w_z} \qquad b_{3z} = \frac{2z'}{w_z}$$

$$a_{4x} = 0 \qquad b_{4x} = \frac{-t_z}{w_x} \qquad a_{4z} = 0 \qquad b_{4z} = \frac{-t_x}{w_z}$$

$$a_{5x} = \frac{1}{w_x} \qquad b_{5x} = \frac{-t_z}{2w_x} + \frac{x'}{w_x} - 1 \qquad a_{5z} = \frac{1}{w_z} \qquad b_{5z} = \frac{-t_x}{2w_z} + \frac{z'}{w_z} - 1$$

Table 5.4 (Cont.)

Case 2: $w_x<t_z<2w_x$ and $w_z<t_x<2w_z$

$$x_1 = x' - (w_x + t_z/2) \qquad z_1 = z' - (w_z + t_x/2)$$
$$x_2 = x' - t_z/2 \qquad z_2 = z' - t_x/2$$
$$x_3 = x' - (w_x - t_z/2) \qquad z_3 = z' - (w_z - t_x/2)$$
$$x_4 = x' + (w_x - t_z/2) \qquad z_4 = z' + (w_z - t_x/2)$$
$$x_5 = x' + t_z/2 \qquad z_5 = z' + t_x/2$$
$$x_6 = x' + (w_x + t_z/2) \qquad z_6 = z' + (w_z + t_x/2)$$

$$a_{1x} = \frac{1}{w_x} \qquad b_{1x} = \frac{t_z}{2w_x} - \frac{x'}{w_x} + 1 \qquad a_{1z} = \frac{1}{w_z} \qquad b_{1z} = \frac{t_x}{2w_z} - \frac{z'}{w_z} + 1$$

$$a_{2x} = \frac{-1}{w_x} \qquad b_{2x} = \frac{-t_z}{2w_x} + \frac{x'}{w_x} + 1 \qquad a_{2z} = \frac{-1}{w_z} \qquad b_{2z} = \frac{-t_x}{2w_z} + \frac{z'}{w_z} + 1$$

$$a_{3x} = \frac{-2}{w_x} \qquad b_{3x} = \frac{2x'}{w_x} \qquad a_{3z} = \frac{-2}{w_z} \qquad b_{3x} = \frac{2z'}{w_z}$$

$$a_{4x} = \frac{-1}{w_x} \qquad b_{4x} = \frac{t_z}{2w_x} + \frac{x'}{w_x} - 1 \qquad a_{4z} = \frac{-1}{w_z} \qquad b_{4z} = \frac{t_x}{2w_z} + \frac{z'}{w_z} - 1$$

$$a_{5x} = \frac{1}{w_x} \qquad b_{5x} = \frac{-t_z}{2w_x} - \frac{x'}{w_x} - 1 \qquad a_{5z} = \frac{1}{w_z} \qquad b_{5z} = \frac{-t_x}{2w_z} - \frac{z'}{w_z} - 1$$

Case 3: $2w_x \le t_z$ and $2w_z \le t_x$

$$x_1 = x' - (w_x + t_z/2) \qquad z_1 = z' - (w_z + t_x/2)$$
$$x_2 = x' - t_z/2 \qquad z_2 = z' - t_x/2$$
$$x_3 = x' + (w_x - t_z/2) \qquad z_3 = z' + (w_z + t_x/2)$$
$$x_4 = x' + (t_z/2 - w_x) \qquad z_4 = z' + (t_x/2 - w_z)$$
$$x_5 = x' + t_z/2 \qquad z_5 = z' + t_x/2$$
$$x_6 = x' + (w_x + t_z/2) \qquad z_6 = z' + (w_z + t_x/2)$$

Table 5.4 (Cont.)

$$a_{1x} = \frac{1}{w_x} \qquad b_{1x} = \frac{t_z}{2w_x} - \frac{x'}{w_x} + 1 \qquad a_{1z} = \frac{1}{w_z} \qquad b_{1z} = \frac{t_x}{2w_z} - \frac{z'}{w_z} + 1$$

$$a_{2x} = \frac{-1}{w_x} \qquad b_{2x} = \frac{-t_z}{2w_x} + \frac{x'}{w_x} + 1 \qquad a_{2z} = \frac{-1}{w_z} \qquad b_{2z} = \frac{-t_x}{2w_z} + \frac{z'}{w_z} + 1$$

$$a_{3x} = 0 \qquad b_{3x} = 0 \qquad a_{3z} = 0 \qquad b_{3z} = 0$$

$$a_{4x} = \frac{-1}{w_x} \qquad b_{4x} = \frac{t_z}{2w_x} + \frac{x'}{w_x} - 1 \qquad a_{4z} = \frac{-1}{w_z} \qquad b_{4z} = \frac{t_x}{2w_z} + \frac{z'}{w_z} - 1$$

$$a_{5x} = \frac{1}{w_x} \qquad b_{5x} = \frac{-t_z}{2w_x} - \frac{x'}{w_x} - 1 \qquad a_{5z} = \frac{1}{w_z} \qquad b_{5z} = \frac{-t_x}{2w_z} - \frac{z'}{w_z} - 1$$

Case 4: a) $w_x < t_z < 2w_x$ and $t_x \leq w_z$

Take a_{jx}, b_{jx}, x_j from Case 2, and take a_{iz}, b_{iz}, z_i from Case 1.

b) $w_z < t_x < 2w_z$ and $t_z \leq w_x$

Take a_{jx}, b_{jx}, x_j from Case 1, and take a_{iz}, b_{iz}, z_i from Case 2.

Case 5: a) $2w_x \leq t_z$ and $t_x \leq w_z$

Take a_{jx}, b_{jx}, x_j from Case 3, and take a_{iz}, b_{iz}, z_i from Case 1.

b) $2w_z \leq t_x$ and $t_z \leq w_x$

Take a_{jx}, b_{jx}, x_j from Case 1, and take a_{iz}, b_{iz}, z_i from Case 3.

Case 6: a) $2w_x \leq t_z$ and $w_z < t_x < 2w_z$

Take a_{jx}, b_{jx}, x_j from Case 3, and take a_{iz}, b_{iz}, z_i from Case 2.

b) $2w_z \leq t_x$ and $w_x < t_z < 2w_x$

Take a_{jx}, b_{jx}, x_j from Case 2, and take a_{iz}, b_{iz}, z_i from Case 3.

Table 5.5. Numerical verification of the analytic expressions for the integral of the asymptotic form. The numerical result is calculated by numerically integrating the spectral domain integrals in (5.14) and (5.15). The analytic result is obtained from the expressions (5.30) and (5.31). The relative position (x',z') of the basis and testing functions is (0.3,0.4). (f=1 GHz, d=1.57 mm, and ε_r=4.0)

Inner Product	w_x	t_x	w_z	t_z	Analytic	Numerical
$\langle \tilde{J}_{xj}, \tilde{G}^a_{xx} \tilde{J}_{xi} \rangle$:	3×10^{-2}	4×10^{-2}	—	—	-7.150×10^{-2}	-7.148×10^{-2}
$\langle \tilde{J}_{xj}, \tilde{G}^a_{xz} \tilde{J}_{zi} \rangle$:						
Case 1	3×10^{-2}	4×10^{-2}	5×10^{-2}	2×10^{-2}	-3.145×10^{-4}	-3.202×10^{-4}
Case 2	"	8×10^{-2}	"	4×10^{-2}	-1.265×10^{-3}	-1.250×10^{-3}
Case 3	"	11×10^{-2}	"	6×10^{-2}	-2.625×10^{-3}	-2.638×10^{-3}
Case 4	"	4×10^{-2}	"	4×10^{-2}	-6.288×10^{-4}	-6.268×10^{-4}
Case 5	"	4×10^{-2}	"	6×10^{-2}	-9.425×10^{-4}	-9.434×10^{-4}
Case 6	"	8×10^{-2}	"	6×10^{-2}	-1.896×10^{-3}	-1.890×10^{-3}

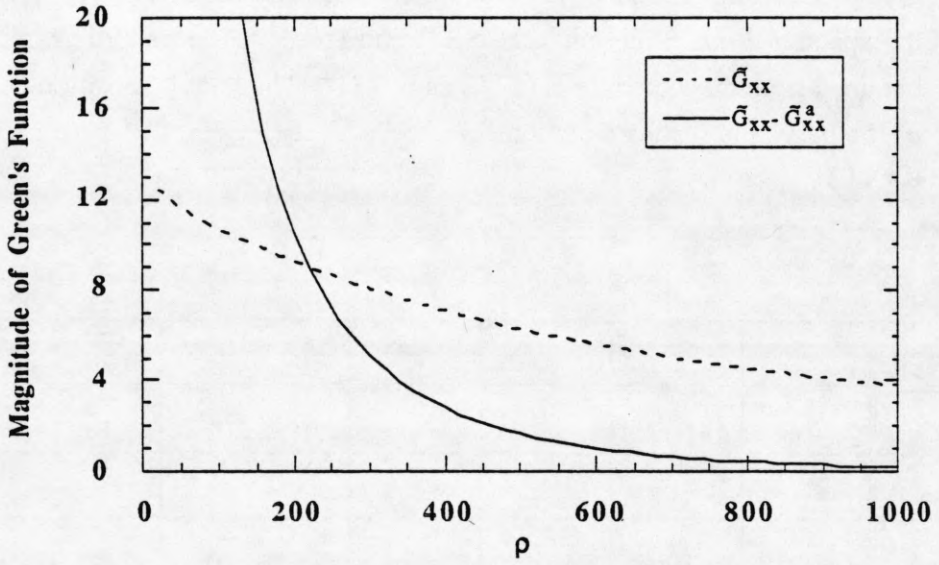

Figure 5.1. Magnitude of the Green's function at $\theta=0^o$ (ε_r=4.0, d=1.57 mm, f=1 GHz).

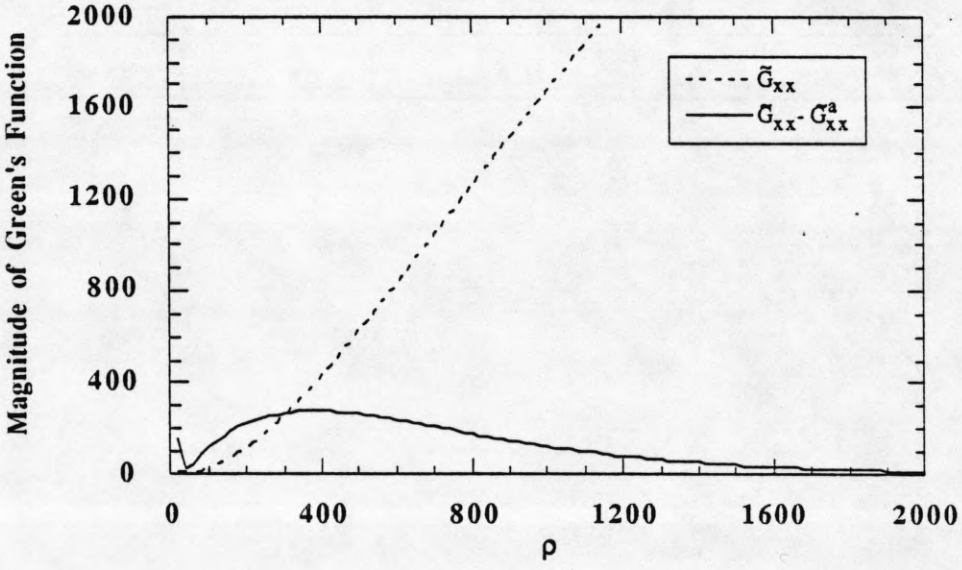

Figure 5.2. Magnitude of the Green's function at $\theta=45^o$ (ε_r=4.0, d=1.57 mm, f=1 GHz).

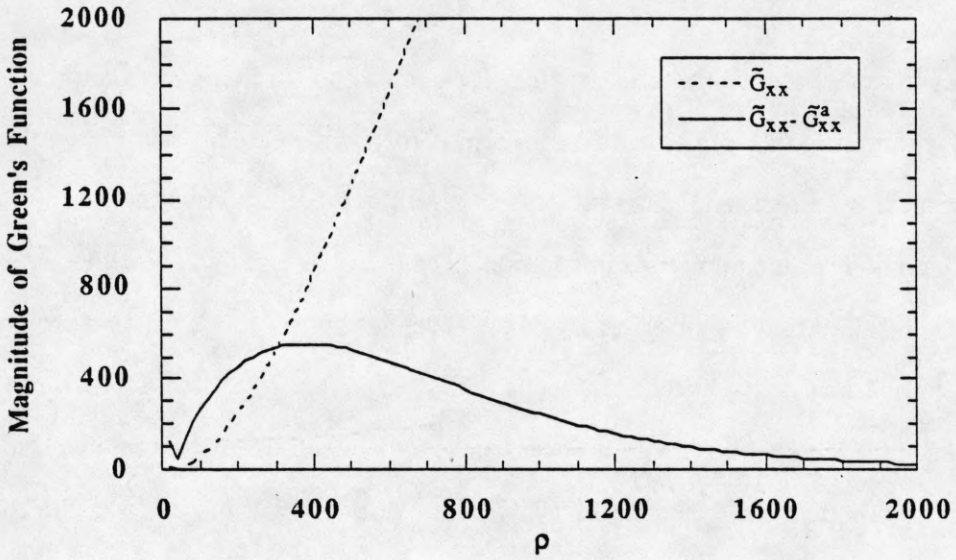

Figure 5.3. Magnitude of the Green's function at $\theta=90^o$ ($\varepsilon_r=4.0$, d=1.57 mm, f=1 GHz).

CHAPTER 6

PERFORMANCE

In this chapter, the asymptotic acceleration technique discussed in Chapter 5 is evaluated by comparing the results of two different algorithms. One algorithm computes the inner products by direct numerical integration, and the other employs the asymptotic acceleration technique in the numerical integration. The direct integration algorithm is used as the standard for determining the accuracy of the acceleration technique. It also provides a basis for a comparison of the execution speeds.

Before comparing the results, it is necessary to understand the numerical integration routines used to compute the inner product integrals. Both algorithms perform the two-dimensional integrations in polar coordinates, and by taking advantage of the symmetry in the integrands, the limits of integration have been reduced to the first quadrant. The integration is implemented numerically by stepping in the theta variable and integrating in rho at each step until convergence. The rho integrations are then summed up over the theta steps with a basic Gaussian quadrature integration routine. For the rho integrations, a general adaptive quadrature routine is used everywhere, except in the region of the singularity. In this region, an adaptive routine designed specifically for singular functions is used.

Defining a good convergence criterion for numerical integrations is a difficult task in general. In this work, the criterion chosen for truncating the infinite rho integrations is based on a relative convergence test. After each step in the rho integration, the most recent approximation to the integral is compared with the approximation from the previous step. If the relative difference is less than a user-specified tolerance, the integration is terminated. The actual procedure implemented requires the integration to satisfy this convergence criterion two consecutive times before terminating.

Although the asymptotic acceleration technique was designed to increase the rate of convergence of the rho integrations, the technique actually accomplishes more than this. In some cases, the inner product evaluation is not possible without the acceleration technique. The reason for this is that the integrand becomes highly oscillatory with respect to theta for large rho. Since the rho integrations are truncated sooner with the acceleration technique, this highly oscillatory region of the integrand may be avoided. It is important to note that the poor asymptotic behavior has been captured analytically in the asymptotic acceleration technique. Therefore, the results obtained with this technique are possibly more reliable than those obtained by direct numerical integration.

As an example of the integrand's poor behavior, the integrand of the inner product $\langle \tilde{J}_{xj}, \tilde{G}_{xx} \tilde{J}_{xi} \rangle$ is plotted with respect to theta in Figures 6.1 and 6.2 for rho at 1000 and 3000. These values of rho are reasonable, since most of the rho integrations cannot be truncated before 3000 for these inner products. From the plots it is apparent that the integrand becomes more oscillatory as rho increases. The behavior of the integrand will also become worse as the separation between the basis and testing functions increases. In Figure 6.1, the separation is approximately a quarter of a wavelength in free space. The behavior of the integrand in Figure 6.2 is substantially worse, where the separation is about a half wavelength. This poor behavior arises from the complex exponential term associated with the basis and testing functions. As a result of this term, the direct integration routine often converges slowly in the theta integration. When the separation is too large, the direct numerical integration completely fails to converge before numerical error dominates.

Since the direct integration of the inner products fails for large separations, the comparison of the algorithms is limited to inner products with relatively small separations. When a comparison is possible, the agreement between the direct and the accelerated evaluations of the inner products is excellent. As an example, consider the case in which the operating frequency is 1 GHz and the dielectric substrate is 1.57 mm thick with a relative dielectric constant of 4. The width and thickness of the basis functions were

chosen to be approximately a twentieth of a free-space wavelength. Several inner products were computed for this case, and the results are given in Table 6.1. The results from the two algorithms are seen to agree very well for the various separations of the source and field points considered. For all of the cases, the complex relative difference is within 3 percent. The largest separation listed is approximately a quarter wavelength. Beyond this distance, the direct integration algorithm did not converge with a reasonable number of points in the theta integration.

Note that the real parts of the inner products in Table 6.1 are identical for the two algorithms, because the asymptotic form only contributes to the imaginary part of the inner product. This brings up the question of the true accuracy of either algorithm. Although the results of the two algorithms are consistent, it is possible that both results may be in error, since the algorithms are based on similar numerical integration routines. However, from the results presented, it is safe to conclude that the asymptotic acceleration technique does not introduce any new error in the evaluation of the inner products.

Finally, the asymptotic acceleration technique is evaluated in terms of its effect on reducing the computation time. For the cases listed in Table 6.1, the acceleration technique provided a speedup that varied between two and four. However, the time saved will increase as the limit of the direct integration is pushed with larger separation distances. The acceleration technique will also be more effective for thicker substrates, since the approximation for the hyperbolic cotangent in the asymptotic form is then better.

The effectiveness of the acceleration technique can also be examined by comparing the maximum rho reached before the convergence criterion is satisfied. In Figure 6.3, an actual path of integration in the first quadrant of the (ρ,θ) plane is plotted for both algorithms. Each radial line represents a rho integration for a particular theta step. For the direct integration, there are a few rho integrations that do not converge until after 5000. In comparison, all of the rho integrations for the accelerated algorithm are seen to converge before 1800. For this example, it appears as though the acceleration technique should

provide a speedup of more than the observed factor of two. The actual reduction in computation time is more modest, because a significant portion of the computation time in each rho integration is spent integrating the singularity adaptively.

Table 6.1 Comparison of the inner products computed using a direct integration algorithm and an accelerated algorithm. The widths and thicknesses of the "rooftop" basis functions are each 0.05 λ_o, and the separation (x′,z′) is given in terms of wavelengths (d=1.57 mm, ε_r=4.0, f=1 GHz).

Inner Product	(x',z')	Direct Evaluation	Accelerated Evaluation
$<\tilde{J}_{xj},\tilde{G}_{xx}\tilde{J}_{xi}>$:	(0,0)	$-2.88\times10^{-5}+j3.84\times10^{-1}$	$-2.88\times10^{-5}+j3.84\times10^{-1}$
	(0.05,0.05)	$-2.80\times10^{-5}-j9.61\times10^{-3}$	$-2.80\times10^{-5}-j9.51\times10^{-3}$
	(0.1,0.1)	$-2.59\times10^{-5}-j1.43\times10^{-4}$	$-2.59\times10^{-5}-j1.44\times10^{-4}$
	(0.2,0.2)	$-1.83\times10^{-5}-j1.05\times10^{-5}$	$-1.83\times10^{-5}-j1.06\times10^{-5}$
$<\tilde{J}_{xj},\tilde{G}_{xz}\tilde{J}_{zi}>$:	(0.05,0.05)	$1.88\times10^{-7}-j6.66\times10^{-2}$	$1.88\times10^{-7}-j6.66\times10^{-2}$
	(0.1,0.1)	$7.21\times10^{-7}+j5.19\times10^{-6}$	$7.21\times10^{-7}+j5.17\times10^{-6}$
	(0.2,0.2)	$2.43\times10^{-6}+j1.30\times10^{-5}$	$2.43\times10^{-6}+j1.34\times10^{-5}$

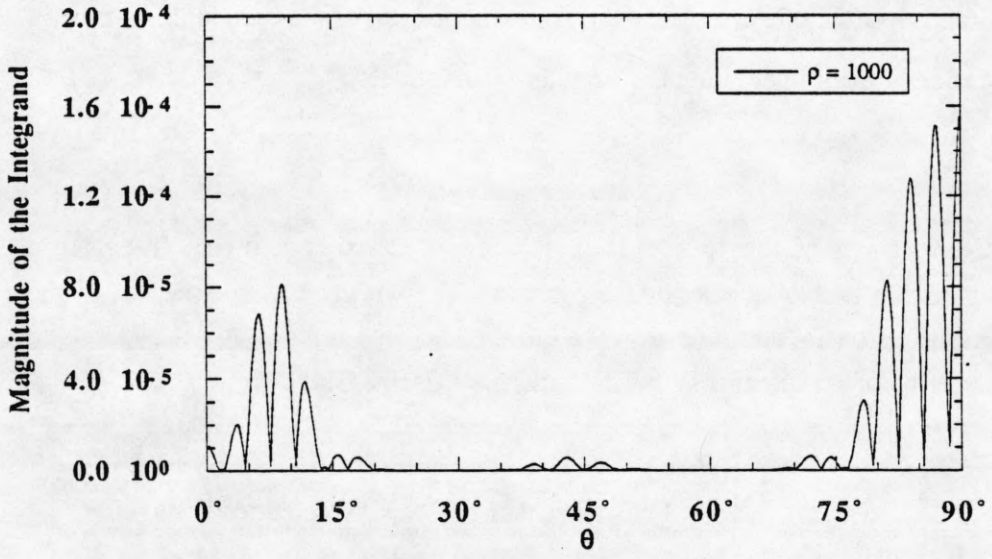

(a) Magnitude of the integrand with respect to θ at ρ=1000.

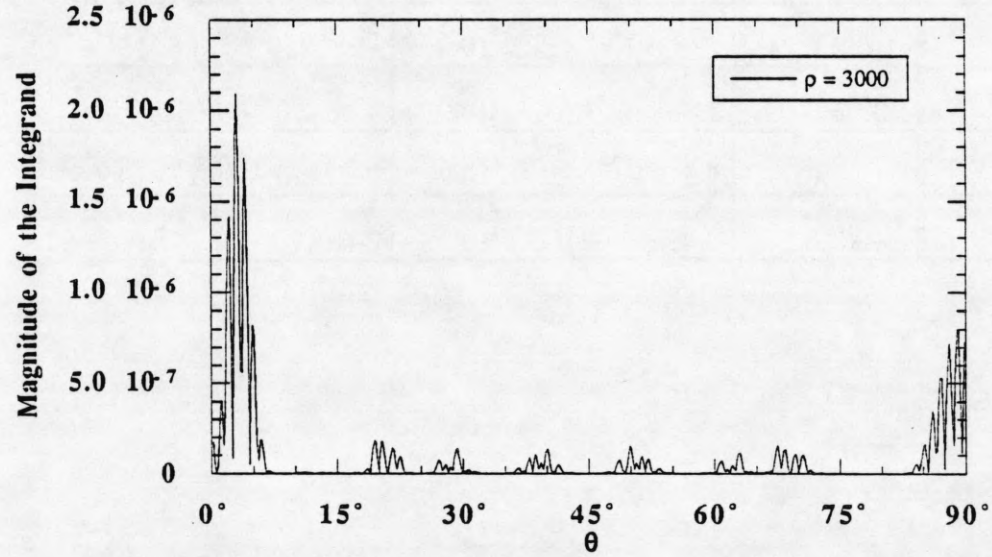

(b) Magnitude of the integrand with respect to θ at ρ=3000.

Figure 6.1 Behavior of the integrand for $\langle \tilde{J}_{xj}, \tilde{G}_{xx} \tilde{J}_{xi} \rangle$ with separation variables x′ and z′ equal to 0.2 λ_o (d=1.57 mm, ε_r=4, f=1 GHz, w_x=t_x=0.05 λ_o).

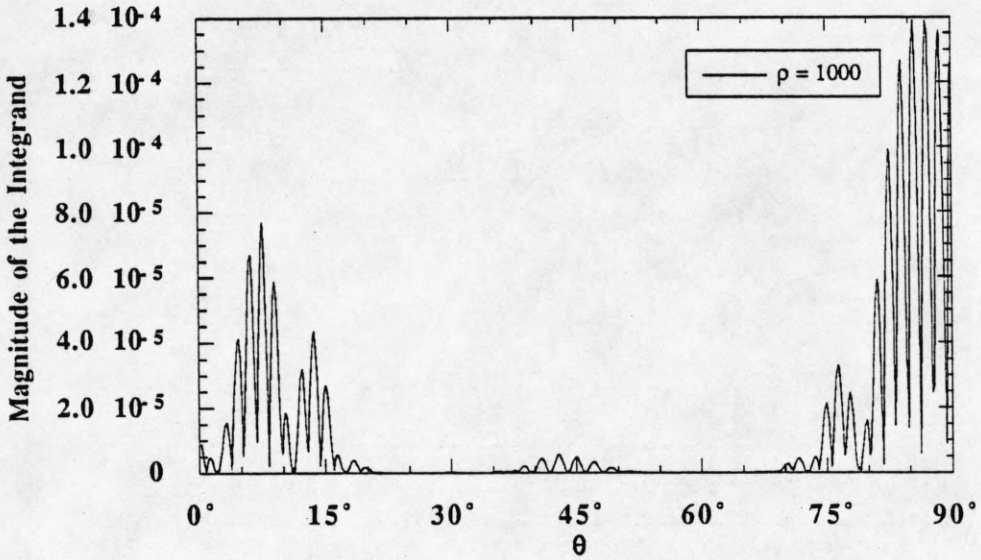

(a) Magnitude of the integrand with respect to θ at ρ=1000.

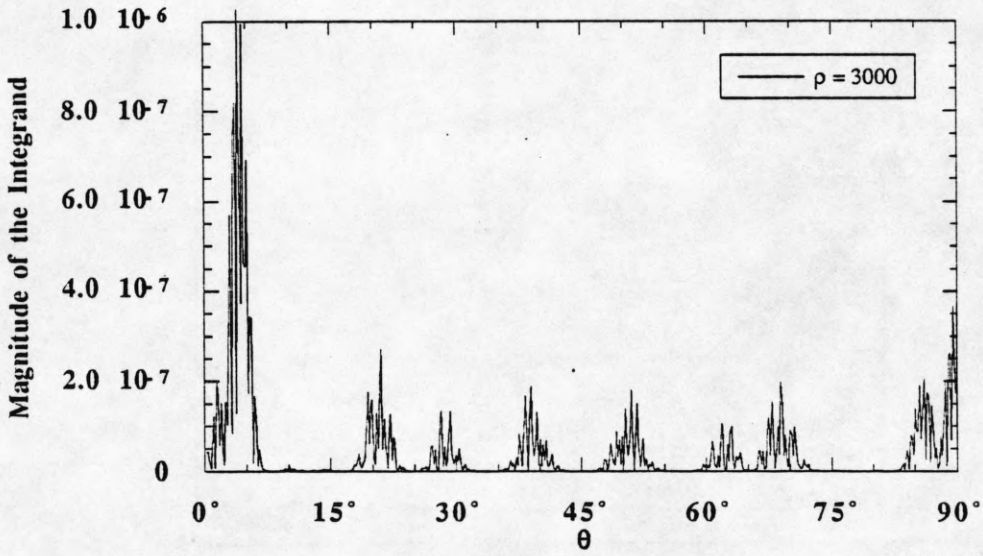

(b) Magnitude of the integrand with respect to θ at ρ=3000.

Figure 6.2 Behavior of the integrand for $\langle \tilde{J}_{xj}, \tilde{G}_{xx} \tilde{J}_{xi} \rangle$ with separation variables x′ and z′ equal to 0.4 λ_o (d=1.57 mm, ε_r=4, f=1 GHz, $w_x=t_x=0.05\ \lambda_o$).

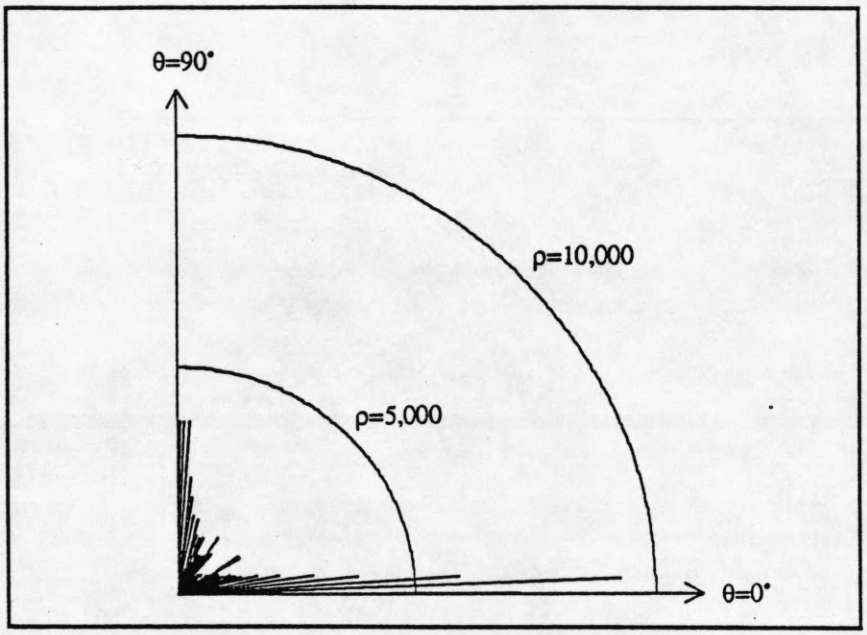

(a) Direct integration algorithm.

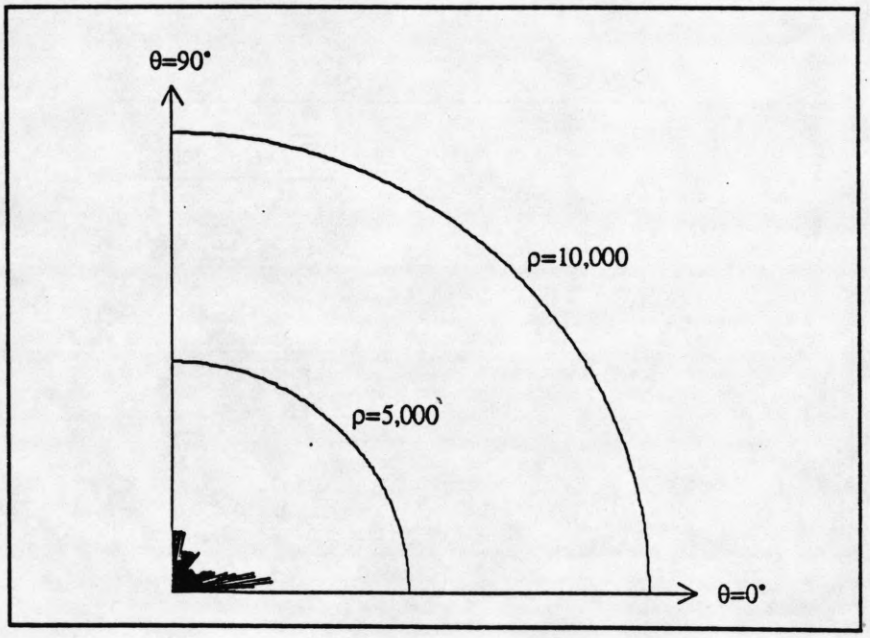

(b) Accelerated algorithm.

Figure 6.3 Integration path in the first quadrant of the (ρ,θ) plane for the inner product $\langle \tilde{J}_{xj}, \tilde{G}_{xx}\tilde{J}_{xi} \rangle$ with separation variables x' and z' equal to 0.2 λ_o (d=1.57 mm, ε_r=4, f=1 GHz, $w_x=t_x=0.05\ \lambda_o$).

CHAPTER 7
CONCLUSIONS

In this thesis the general microstrip discontinuity problem was formulated in the spectral domain. The moment method was then used to generate a set of algebraic equations that could be solved numerically. When this procedure was implemented, it was found that there were numerical difficulties associated with the evaluation of the inner products. One such difficulty was the numerical integration of the singularities corresponding to the surface wave poles. The nature of these singularities and possible methods to integrate them were discussed. Another difficulty encountered was the slow convergence rate of the inner product integrals. The convergence rate of these integrals was improved by applying an asymptotic acceleration technique. In this work, the integral of the asymptotic form was derived analytically in closed form; therefore, the maximum speedup was achieved for the asymptotic extraction. Also, no additional error was introduced in the computation.

In order to evaluate the effectiveness of the asymptotic acceleration technique, two different algorithms were developed. One algorithm employed the acceleration technique in the evaluation of the inner products, and the other computed the inner products by direct numerical integration. Both routines took advantage of symmetry in the integrands to obtain an initial speedup. The results from the two algorithms were in close agreement, confirming the fact that the acceleration technique does not compromise the accuracy. For the cases considered, the acceleration technique reduced the overall computation time by a factor that varied between two and four. It was also found that the acceleration technique allowed certain inner products to be evaluated numerically that appeared to be unattainable with the direct integration routine.

Although the asymptotic acceleration technique was developed for the microstrip discontinuity problem, it should be noted that the technique is also useful in the spectral

domain analysis of other grounded dielectric slab structures. In particular, patch antennas, printed dipoles, and disk resonators can be analyzed using this technique.

The work to improve the efficiency of the inner product evaluation is far from complete. Several potential improvements on the technique should be investigated in the future. For instance, the acceleration technique could easily be implemented in conjunction with higher-order basis functions to further enhance the convergence rate of the inner product integrals. In addition, the use of higher-order asymptotic forms in the acceleration technique should be considered. In the latter case, an analytic evaluation of the resulting asymptotic integrals may not be possible, but approximations may exist (i.e., series expansions) for which the tradeoffs between computation time and accuracy are acceptable. Finally, the computation time could be reduced significantly if a more efficient method of integrating the singularities were implemented.

REFERENCES

[1] P.B. Katehi and N.C. Alexopoulos, "Frequency-dependent characteristics of microstrip discontinuities in millimeter-wave integrated circuits," *IEEE Trans. Microwave Theory Tech.*, vol. MTT-33, pp. 1029-1035, Oct. 1985.

[2] R.W. Jackson and D.M. Pozar, "Microstrip open-end and gap discontinuities," *IEEE Trans. Microwave Theory Tech.*, vol. MTT-33, pp. 1036-1042, Oct. 1985.

[3] N.H.L. Koster and R.H. Jansen, "The microstrip step discontinuity: A revised description," *IEEE Trans. Microwave Theory Tech.*, vol. MTT-34, pp. 213-223, Feb. 1986.

[4] R.W. Jackson, "Full-wave, finite element analysis of irregular microstrip discontinuities," *IEEE Trans. Microwave Theory Tech.*, vol. 37, pp. 81-89, 1989.

[5] T. Itoh, "Spectral domain immitance approach for dispersion characteristics of generalized printed transmission lines," *IEEE Trans. Microwave Theory Tech.*, vol. MTT-28, pp. 733-737, July 1980.

[6] T. Itoh and W. Menzel, "A full-wave analysis method for open microstrip structures," *IEEE Trans. Antennas Propagat.*, vol. AP-29, pp. 63-68, Jan. 1981.

[7] S.M. Wright, "Efficient analysis of infinite microstrip arrays on electrically thick substrates," Ph.D. dissertation, University of Illinois, Urbana, Illinois, 1984.

[8] R.F. Harrington, *Field Computation by Moment Methods*. New York: Macmillan, 1968.

[9] N.K. Uzunoglu, N.G. Alexopoulos, and J.G. Fikioris, "Radiation properties of microstrip dipoles," *IEEE Trans. Antennas Propagat.*, vol. AP-27, pp. 853-858, Nov. 1979.

[10] R.V. Churchill and J.W. Brown, *Complex Variables and Applications*. New York: McGraw-Hill Book Company, 1984, pp. 94-95.

[11] R.F. Harrington, *Time-Harmonic Electromagnetic Fields*. New York: McGraw-Hill Book Company, 1961, pp. 116-118.

[12] R.V. Churchill and J.W. Brown, *Complex Variables and Applications*. New York: McGraw-Hill Book Company, 1984, pp. 43-46.

[13] M.L. Oberhart, private communication at the University of Illinois.